2014

Inverted Linear Halbach Array for Separation of Magnetic Nanoparticles

Chetan Poudel
Oberlin College

Oberlin College

Honors Thesis

Inverted Linear Halbach Array for Separation of Magnetic Nanoparticles

Author:
Chetan Poudel

Advisor:
Dr. Yumi Ijiri

A thesis submitted in fulfillment of the requirements for the Honors program in Physics

in the

Department of Physics and Astronomy

May 2014

Executive Summary

Inverted Linear Halbach Array for Separation of Magnetic Nanoparticles

by Chetan Poudel

Magnetic nanoparticles are extremely tiny particles that act like compass needles in that they can be influenced by larger magnets. These nanoparticles can in turn interact with other particles near them, influencing their directions and arrangements. Usually, these particles are suspended in a fluid for use in biomedical applications. However, most of these applications can work well only if we can ensure that these particles are uniform, not just in their size but also in their magnetic properties. Therefore, separations and purifications of these particles are of utmost importance if we are to make use of these applications.

In this thesis, we describe our creation of a new device and method for separating magnetic nanoparticles. This device uses a special arrangement of magnets that can influence a mixture of particles flowing on top of them. This influence causes larger and more magnetic particles to separate away from the smaller and less magnetic particles. Therefore, upon flowing one mixture containing small and large particles through the device, one can obtain two separated solutions: one with only small particles and one with only large particles, both more uniform than the mixture we started out with.

We investigate the separation process by first examining the general interactions of nanoparticles with magnets. We also describe in detail how we investigate the properties of the nanoparticle mixtures. In our experiments, we find that the device can separate some types of particle mixtures fully and some only partially. We try to explain why this may be so. Finally, we establish how efficiently the device performs and the ways to improve its performance in future experiments. We conclude by mentioning ongoing and future work that could be done to enhance the workings of our device to reach our goal of separating nanoparticles for use in desired biomedical applications.

Acknowledgements

I would first and foremost like to extend my deepest gratitude to my advisor, Professor Yumi Ijiri, for giving me the opportunity to work in her lab. Her guidance, teaching, encouragement and her patience in letting me figure out scientific problems and conduct experiments on my own have been invaluable to my growth as a researcher. I also very much appreciate the time she put into helping me edit most of the writing in this thesis.

I would also like to thank my lab partner, Kathryn Hasz, for being a great friend throughout. Thanks for all the baked desserts and for putting up with, and perhaps even enjoying, my pop music and strange ideas in lab. Many thanks also for her help with developing a new framework to analyze my experimental data.

In addition, I would like to thank my other wonderful physics friends Dagmawi Gebreselasse, David Morris, Jocienne Nelson, Ben Lemberger, Elizabeth Garbee, Zach Mark, Sujoy Bhattacharya, Mattie Dedoes, Noah Jones, Mike Rowan, Elizabeth Gilmour and Sam Berney for spending many nights tackling arduous problems sets together and for all the fun we had in Wright. Thanks to the juniors Greg Stevens, Cooper McDonald, Donal Sheets, Dan Bloch, Dan Barella and Dan Laufer for the amusing discussions. I would also like to acknowledge Jason Stalnaker and all other professors of the Oberlin Physics department for being such excellent resources and perpetually challenging and stretching my knowledge. Thanks to Bill Marton for his excellent machining work on many projects and to Diane for taking care of us all.

Many thanks to my girlfriend Valerie Feerer for her love and to my housemates and friends Cuyler, Tania, Clara, Pete, Steve, Ren and Shiva for keeping me going. Finally, I am very grateful for the constant encouragement and frequent calls from my loving family and relatives, while I lived thousands of miles away and kept staying at Oberlin for many summers and winters doing research without coming home.

This work was partially supported by NSF grant DMR-1104489, NIH CA62349, a Great Lakes College Association New Directions Initiative Award, the Cleveland Clinic, and an Oberlin College Research Status Award. The research made use of equipment obtained from NSF DMR-0922588 and DUE-9950606.

Contents

List of Figures

List of Tables

Abbreviations

MRI	**M**agnetic **R**esonance **I**maging
MRI	**M**agnetic **P**article **I**maging
HGMS	**H**igh **G**radient **M**agnetic **S**eparation
MgFFF	**Mg**netic **F**ield **F**low **F**ractionation
DMCR	**D**ifferential **M**agnetic **C**atch and **R**elease
ElFFF	**El**ectric **F**ield **F**low **F**ractionation
NdFeB	**N**eo**d**ymium **Fe**rrum(Iron) **B**oron
SAXS	**S**mall **A**ngle **X**-ray **S**cattering
SANS	**S**mall **A**ngle **N**eutron **S**cattering
XRD	**X**-**R**ay **D**iffraction
FEMM	**F**inite **E**lement **M**ethod **M**agnetics
CAD	**C**omputer Aided **D**esign
TEM	**T**ransmission **E**lectron **M**icroscopy
VSM	**V**ibrating **S**ample **M**agnetometer
NSF	**N**ational **S**cience **F**oundation
NIST	**N**ational **I**nstitute of **S**cience and **T**echnology

Symbols and Units

$\mathbf{m}$	magnetic moment	emu or erg/gauss
$\mathbf{M}$	mass magnetization	emu/g
$\mathbf{H}$	applied magnetic field	Oersted(Oe)
$\mathbf{B}$	magnetic flux density	Gauss
χ	magnetic susceptibility	dimensionless
K	magnetic anisotropy	erg/cm^3
Φ	magnetic flux	maxwell
σ	saturation magnetization	emu/g
F_m	magnetic force	erg
η	viscosity	centipoise (cP)
v_p	velocity of particle	μm/s
$\mathbf{Q}$	scattering vector	Angstrom^{-1} or Å^{-1}
$\mathrm{I}(\mathbf{Q})$	scattering intensity	arbitrary units

Glossary and Physical Constants

Boltzmann's constant	k_B	=	1.38×10^{-23} J/K
Permeability of vacuum	μ_0	=	$4\pi \times 10^{-7}$ N/A^2 in SI or 1 in CGS
Avogadro's constant	N_A	=	$6.022\ 136\ 7(36) \times 10^{23}$ mol^{-1}
Bohr magneton	μ_b	=	9.27×10^{-21} emu
Room temperature	T	=	298 K
Viscosity of toluene	$\eta_{toluene}$	=	0.580 cP
Viscosity of water	η_{water}	=	1.00 cP at room temperature

Dedicated to Buwa, Baba, Mamu and Saugat...

Chapter 1

Motivation and Approach

1.1 Colloidal magnetic fluids and nanoparticles

Magnetic fluids are stable colloidal suspensions of nano-sized particles of magnetic materials in a carrier liquid. Such artificial strongly magnetic fluids were first synthesized in the 1960s, with an unprecedented amount of research that followed in later years [1, 2]. The small size and magnetic characteristics of these nanoparticles in fluid have opened up a wide range of very interesting and promising applications, especially in biomedicine.

Biomedical nanomagnetics is the name given to the multidisciplinary research area studying magnetic nanoparticles for their applications in diagnostic imaging, targeted drug delivery, cancer therapy and hyperthermia [3]. The nanometer dimensions of these particles allow them to interact with biological entities like cells and molecules. The nanoparticles can be coated with some specific biomolecules to allow uptake into the body and for selective interactions with other biomolecules. The nanoparticles can also be tagged with fluorescent markers (like green fluorescent proteins) and be attached to selected cells for optical imaging [4]. Some nanoparticles also form excellent contrast agents for *in vitro* magnetic resonance imaging (MRI) or magnetic particle imaging (MPI) [5]. The nanoparticles can be manipulated with external field gradients to for guide the transport of drugs or genes to targeted sites in the body [6]. Introducing and attaching colloidal magnetic nanoparticles, whose magnetic susceptibility exceeds that of other intact cells by several orders of magnitude, into some biological membranes offers magnetic control of selected cells from the outside. Magnetic nanoparticles also respond to an alternating or time-varying

magnetic field, with an advantageous transfer of energy from an exciting field to the nanoparticle. This release of energy can be exploited to heat up the particles and surrounding tissue by heat transfer. This technique in cancer therapy, which is called hyperthermia, can strongly supplement chemotherapy, destroying tumor tissues in a localized fashion inside the body [7].

In all major clinical applications of magnetic fluids, the ability to control important parameters like imaging resolution, payload delivery, transport efficiency and temperature is crucial. Achieving this control depends critically upon the ability to obtain superior quality nanoparticle samples, with high uniformity in particle size and in magnetic properties. This is because a non-uniform distribution of billions of particles will cause the response of a certain group of particles to be vastly different from other particles in the same sample, causing uncontrolled and unintended consequences. There is an obvious advantage in having a narrow distribution in particle-size and magnetization since large deviations can adversely affect the performance, especially in applications where the nanoparticles are subjected to large fields or field gradients.

However, the synthesis of nanoparticles for use in these applications is a difficult and sensitive chemical process that requires a judicious selection of reaction conditions to promote nucleation on preformed nanocrystal seeds into the final product. Even then, a number of parameters in the synthesis like heating temperature, seed size, seed crystallinity, solvent polarity, stabilizer concentration all influence the final product morphology [8]. Some highly optimized syntheses of nanoparticles can and have yielded samples with very narrow size distributions but the problem of irreproducibility of similar 'monodisperse' samples is often-overlooked in these syntheses. It might also be the case that even though samples appear to be monodisperse in size, heterogeneities still exist in composition and crystallinity among particles in the solution. In the absence of methods for accessing and assuring the purity of these synthesized products, the ultimate use of magnetic nanoparticles in biomedical applications cannot be validated and therefore is likely to be limited. Therefore, post-synthesis purification and separation is of paramount importance for expanding the potentials of magnetic nanoparticles in medical and biodiagnostic applications.

1.2 Separation of magnetic nanoparticles

Unfortunately, post-synthetic separation and purification methods for use with small colloidal nanoparticles are scarce in nanoparticle synthesis literature. There exist comparatively only a few sorting methods, which are typically quite tedious, and even then mostly based on size-based selection and not based on magnetic characteristics. The application of analytical separations has largely been limited to larger micron-sized particles and biological cells despite the promising applications of smaller nanoparticles in emerging technologies. Even while some nanoparticle purification methodologies exist, a well-quantified and characterized separation of colloidal nanoparticles is rarely practiced. We briefly review the few existing techniques and methods used in purification or separation of magnetic nanoparticles, first starting with magnetic-based methods using magnetic fields and gradients of simple magnets, high gradient magnetic separation (HGMS), magnetic field flow fractionation (MgFFF), and differential magnetic catch and release (DMCR). We then briefly explore the manipulation of nanoparticles using microfluidic channels, electric fields and other solely size-based separation techniques.

Most separation procedures of magnetic nanoparticles involve recovery or control of the motion of the superparamagnetic particles and so magnetophoresis is an essential step, for which magnetic gradients are employed. The simplest and crudest way to do this would be to use a simple permanent magnet near a nanoparticle suspension. The problem with a simple magnet is the high field and low gradient it provides, magnetizing and accumulating all particles towards it, without any selective sorting criteria. If this magnet is placed sufficiently far enough to cause a weak field to magnetize only the more magnetic particles, the field gradient which influences the magnetophoretic particle velocities becomes so low that the process of separation takes an incredibly long time (a few days for one sample), making it very inconvenient or of not much use.

Some better methods like high gradient magnetic separation (HGMS), magnetic field flow fractionation (MgFFF) and differential magnetic catch and release (DMCR) use flow based techniques in conjunction with applied magnetic fields [9]. HGMS methods use various flow channel geometries and columns packed with micron sized magnetic wires that can be magnetized with a powerful electromagnet to create very inhomogeneous magnetic fields of 1 to 2 Tesla with a high gradient (greater than 1000 T/m) for high throughput. HGMS is common in separation of micron-scale or

larger particles but a similar theoretical framework could be utilized for separation of magnetic nanoparticles [10]. HGMS is best suited for separating nanoparticles out of a mixture of magnetic and non-magnetic particles, in applications relating to water purification and removal of toxic waste [11], and not so much for sorting between two different particle distributions originating from the same mixture. That is because even through HGMS guarantees high magnetophoretic particle velocity, the high gradient sources necessarily consist of a large field that magnetizes all particles and causes them all to be trapped in the separating column, without enough sensitivity to discriminate between particles in the mixture [12]. A research group [13] has recently demonstrated good separation efficiency and yield in sorting several different populations from a complex mixture of nanoparticles less than 20 nm in size using variable field applications in a conventional HGMS. This is an exciting result for the use of an HGMS method, but they too report difficulties with separating larger nanocrystals from each other.

MgFFF is another separation and characterization technique, which is better for sorting of magnetic nanoparticles in that it can distinguish different magnetic particle components that vary in their magnetic material content from the same mixture [14]. In MgFFF, the interplay of hydrodynamic and magnetic forces elutes magnetic particles at different times at the outlet (similar to a chromatography technique) as they flow along a thin, parallel-walled channel, on which a magnetic field or gradient is applied perpendicularly. Knowing the magnetic properties of the core material, MgFFF can be used to roughly calculate the size distribution as well as the mean size of magnetic cores of particles. However, careful examination of this method reveals a number of significant problems. MgFFF involves indirect characterization of the particles using calculations of observed elution time [15]. Such indirect size distribution calculations are only accurate to the extent that particle size scales with the core size. If most particles in the sample have a magnetically dead layer while still being large in size, MgFFF will tend to underestimate the sample's average particle size. Multiple MgFFF attempts have also failed because of difficulty in creating uniform field arrangements throughout the channel. Some groups have used a quadrupole MgFFF system [10, 16] to create uniform radially symmetric regions in the flow channel to remedy this problem but it stills seem to work best only for bigger nanoparticles hundreds of nanometers in diameter. Being able to sort smaller nanoparticles in the 5 nm - 50 nm range would be much more desirable for biomedical applications in cellular transport and magnetic targeting.

Differential magnetic catch and release (DMCR) is a relatively new technique [17] that tries to focus on separating polydisperse magnetic nanoparticles with sizes less than 20 nm into monodisperse fractions that are compatible for bioanalysis and medical applications. DMCR separates particles in the mobile phase using differential applied magnetic forces to trap and retain flowing nanoparticles against the wall of an open tubular capillary wrapped between two narrowly spaced electromagnetic poles. Despite the method's successful demonstration of separation of three sizes of magnetic nanoparticles with small differences in diameter and of reduction in size distribution of particles, there are a number of problems that arise in this technique as well. First of all, it uses very high tunable fields in the order of Teslas that requires a powerful expensive electromagnet using high voltage and chillers. On the other hand, this method uses an injection volume of $\sim$1 μL and separates the volume into monodisperse fractions in around 25 to 100 minutes [18]. This would take a thousand times longer to separate usable milliliter amounts of sample, especially if the yields of nanoparticles are as low as reported. Therefore, it seems to be a good process for demonstrating magnetic separation but is in no way a time efficient or easily scalable technique.

Another large research area where size-based and magnetic nanoparticle separations have been tested is in microfluidics or "lab on a chip" technologies. These microchannels allow analysis of exceedingly small quantities of sample with low cost, portability and remarkable high resolution [9]. Descroix and co-workers [19] developed a microchip for trapping and releasing 30 nm diameter iron oxide nanoparticles at high gradient and flow rates of tens of μL in an hour. Taking heed of the throughput rate, we can very well see that although microfluidics may be useful to obtain minuscule amounts of very uniform samples, it cannot be utilized for manipulation of particle solutions in large scales. Electric field flow fraction (ElFFF) methods [20] using electric fields for elution-based separations of nanoparticles are also of increasing use but they suffer from other limitations in that only size-based separation of large charged nanoparticles are possible. Even small pH changes or changes in solvent and surface chemistry can result in aggregation, degradation in these methods. Similarly, there are various other methods of fine size separation for nanomaterials including centrifugation [21], salts-based selective precipitation [22], size exclusion chromatography [23], and diafiltration [24], but these processes do not take advantage of the magnetic properties of iron oxide nanoparticles and are thus of limited use in creating samples for use in magnetic field based biomedical applications.

Although quite a bit of research work on nanoparticle separations has been done, we can clearly see that a well-characterized and high-throughput separation of colloidal magnetic nanoparticles in a size regime where they can be of great use to biomedical applications is rarely practiced.

1.3 Introduction and applications of the Halbach magnet array

Our research project considers a novel idea to fill these gaps in the field of size-based and magnetic separation of small colloidal nanoparticle suspensions, utilizing a well-established technology cleverly refashioned to suit our purpose of nanoparticle sorting. Our method also employs rigorous and well-defined characterization of nanoparticle suspensions throughout the process to quantify separation success. The aim of the project is simple: to take nanoparticle samples with particle sizes varying from around 5 nm to 30 nm synthesized without magnetic and size uniformity and transform them into uniform well-characterized samples usable for aforementioned important biomedical applications.

Our idea came out of research work in tailored high magnetic fields and high flux used by Klaus Halbach [25] in designing synchrotron magnets, and in magnetic levitation systems. The importance of tailored homogeneous fields and gradients to magnetic sorting technology has already been established before. While such adjustable field sources are typically electromagnets powered by large amounts of power (typically more than a thousand watts and a chiller to keep the electromagnet from heating) [26], the discovery of Neodymium Iron Boron (NdFeB) permanent magnets with high coercivity and remanence properties made them viable alternatives to powered sources for these same applications [27]. We examined an important class of such permanent magnet designs described by Mallinson [28], based on a particular arrangement of permanent magnets in an alternating pattern. This special arrangement gave the design a unique and counter-intuitive ability to confine most of the magnetic flux to only one side of the design while keeping the magnetic field profile considerably more spatially uniform throughout the structure on either face compared to simpler magnet arrays. Mallinson showed the field would be confined in this way if the component of magnetization were any Hilbert transform pair, the

simplest of which is $\mathbf{v} = \sin(\mathrm{x})\hat{i} + \cos(\mathrm{x})\hat{j}$, where $\mathbf{v}$ is the magnetization vector and x is the position along the design.

The concept of one-sided flux structures, now referred to as 'Halbach arrays', is not new. Many of its characteristics are known in the context of devices such as magnetic recording tape, refrigerator magnets, and even in drug targeting and cell separation [29]. One proposed usage of Halbach arrays is in creating a magnetic bandage for targeting and controlling the delivery of therapeutic agents into tumor sites. Research groups [30, 31] have discovered that a Halbach array configuration of magnets placed near a small tumor yields the best trapping characteristics (large and uniform force distributions) and maximal pulling and pushing forces, outperforming benchmark magnets of similar size and strength, to magnetostatically control small highly magnetic particles injected into the region of interest. The particles could then slowly release chemotherapeutic drugs, or radiate tissues using beta emitters in them or induce localized hyperthermia on application of an alternating magnetic field. When the Halbach array is finally removed, the particles redistribute into the blood supply and then be cleared out. Halbach arrays have recently also been used to continuously sort micrometer-sized magnetic particles with a fluid channel placed over the high flux side of the array [32].

However, to the best of my knowledge, the low flux side of the Halbach array has never been previously considered for any purpose. Our investigations have revealed that the low flux side of the array contains two things that are rarely seen in conjunction: a low field value coupled with large field gradients over single magnet arrangements. In addition, the linear Halbach arrangement we created through appropriate modulation of the magnetization vectors of individual magnets produced substantially uniform fields and gradients for planes parallel to the array. We have found that these field and gradient profiles can be exploited to perform well-characterized and replicable procedures of magnetic separations of nanoparticles in the size range of a few nanometers, which as we described earlier, is an ideal size range for many biomedical applications of nanoparticles.

In the next few chapters, we will delve into the particulars of our magnetic separation approach using the aforementioned advantages of the low flux side or inverted side of the Halbach array. In Chapter 2, we will develop a theoretical framework to understand the responses of nanoparticles in magnetic fields and the underlying physics used in magnetic separation. In Chapter 3, we will go into the details of

design, construction and characterization of the Halbach array fashioned for our separation purpose. Chapter 4 will include discussions of the nanoparticle samples we used, and the experimental setup and procedures used in the collection and characterization of our data. In Chapter 5, we will present and analyze our results from typical experiments performed using the array and the importance of those results. We will also provide a quantified analysis of the device performance using data from all our separation experiments to inform the reader of ways to maximize separation efficiency in future experiments. We conclude in Chapter 6 by briefly recounting our separation method and its utility, our most important results, and the future work that could to be done to firmly establish and expand on some of our exciting results.

Chapter 2

Theory

This chapter reviews the fundamental theory of magnetism and the special case of nanoparticle magnetism to understand the theory behind our magnetic separation approach. Later, particular attention is paid to explaining the theoretical basis for small angle x-ray scattering measurements that constitute our primary analysis method.

2.1 Types of magnetism

To understand in detail how a magnetic sorting approach might work, we first review the fundamental concepts of magnetism to understand the responses of magnetic nanoparticles in the presence of magnetic fields [33]. Further details can be found in one of the many books on magnetism [34, 35, 36].

All materials are magnetic to some extent, with their magnetic responses depending upon the material's atomic structure and temperature. The magnetization of these materials is given by the vector sum of all individual magnetic moments $\mathbf{m}$ in a volume V of the material:

$$\mathbf{M} = \frac{\Sigma \mathbf{m}}{V} \tag{2.1}$$

If any material is placed in an applied magnetic field of strength $\mathbf{H}$, the individual atomic moments in the material will contribute to its overall response called the magnetic induction $\mathbf{B}$ where:

$$\mathbf{B} = \mu_0(\mathbf{H} + \mathbf{M}) \tag{2.2}$$

and μ_0 is the permeability of free space. All materials may then be conveniently classified in terms of a tensor called their volumetric magnetic susceptibility χ, where

$$\mathbf{M} = \chi \mathbf{H} \tag{2.3}$$

describes the magnetization induced in a material by $\mathbf{H}$. In CGS units, χ is dimensionless, $\mathbf{B}$ is measured in Gauss(G), $\mathbf{H}$ in Oersted(Oe) and mass magnetization $\mathbf{M}$ in emu/g. Materials show a wide range of magnetic behavior, with most only exhibiting weak magnetism, and even then only in the presence of an external applied magnetic field. These are particles with non-interacting spins characterized by a linear susceptibility, classified either as paramagnets (PM), for which χ falls in the range 10^{-6} to 10^{-1}, or as diamagnets (DM), with χ in the range -10^{-6} to -10^{-3}, whose $\mathbf{M}$ vs. $\mathbf{H}$ curves are shown in Figure 2.1 (A), (B).

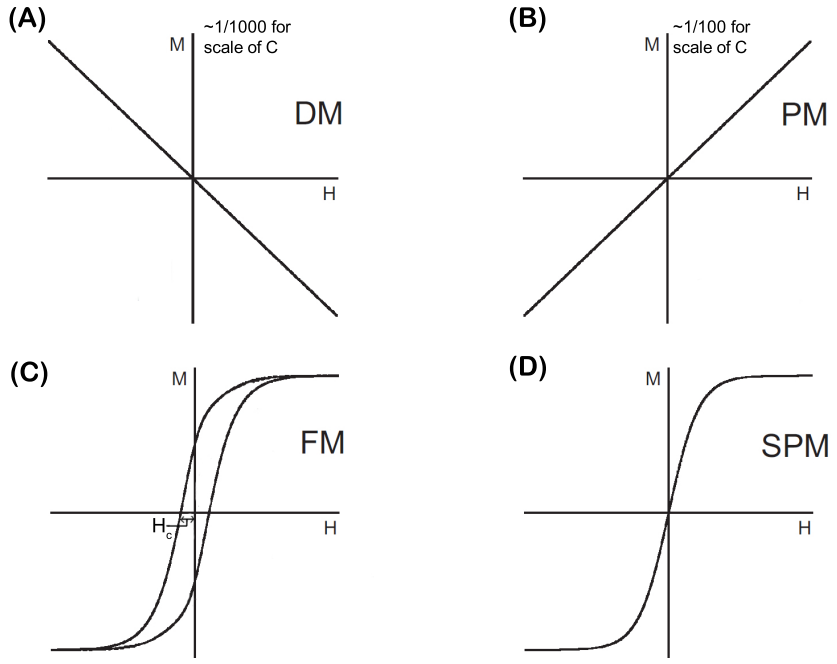

Figure 2.1: Magnetic responses associated with different classes of magnetic materials. $\mathbf{M}$ vs. $\mathbf{H}$ curves are shown for diamagnetic (DM) and paramagnetic (PM) materials, for multidomain larger ferromagnetic (FM) particles and for small nanometer-sized superparamagnetic (SPM) particles.

However, some materials are magnetic even without an applied field and can be viewed as a collection of various magnetic regions called domains, separated by domain walls, with each domain consisting of moments lined up in a certain direction with respect to the external applied field, as shown in Figure 2.2.

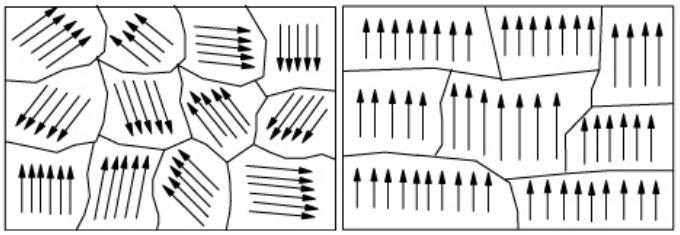

Figure 2.2: Magnetic domains of ferromagnetic materials in the absence (left) and presence (right) of a strong applied magnetic field in the upward direction. There are differences in size and number of domains in the two cases.

These materials exhibit ordered magnetic states, interactions between individual moments, and a finite intrinsic coercivity H_c which refers to how strongly the material resists demagnetization, given by the magnitude of external field applied in a reverse direction to bring the magnetization from saturation back to zero, shown in Figure 2.1 (C). Another distinguishing feature is that the **M** vs. **H** curves of these materials exhibit hysteresis - the material follows a different curve during demagnetization than it does when being magnetized, leading to a closed loop as shown in Figure 2.1 (FM). This hysteretic behavior is caused due to rotation in magnetization of moments and change in size or number of magnetic domains when the applied field is increased, which isn't exactly reversed when the applied field is later decreased. The materials exhibiting these properties are classified as ferromagnets, where the prefix refers to the nature of the coupling interaction between the electrons within the material. This coupling can give rise to large spontaneous magnetizations; in ferromagnets **M** is typically 10^4 times larger than would appear otherwise.

2.2 Superparamagnetism

If we now reduce the size of ferromagnetic materials to length scales of domain wall widths or nanometer dimensions, we ultimately reach a size where it is more energetically favorable for the particle to first have a single magnetic domain. Then the thermal energy ($k_BT = 4.01 \times 10^{-21}$ J, at T=300 K where k_B is the Boltzmann constant of value 1.38×10^{-23}J/K) becomes greater than the anisotropy energy barrier KV (where K is the magnetic anisotropy of the material and V is the volume of the particle), causing the magnetization direction of the nanoparticle to randomize. The anisotropy energy barrier for a small magnetic particle, which is the energy that must be exceeded to cause magnetic direction reversal by a spin-flip, is loosely

speaking, a product of the square of the saturation magnetization (**M**) and its volume ($V \sim d^3$) [37]. As a first approximation of the characteristic particle size when this spin-flip energy barrier is attained, we can set the simple magnetization reversal energy equal to the thermal energy, i.e. $M^2d^3 \sim k_BT \sim 4.01 \times 10^{-21}$ J at room temperature. For typical nanosized ferromagnets, we can obtain a characteristic length of diameters less than 30 nm, below which ferromagnetism gives way to this unique behavior such that when no external magnetic field is applied, the average magnetization measured in a finite time interval (typically, 100 s) is zero. Such materials show no intrinsic coercivity and behave as paramagnets with a huge moment, which is why they are called superparamagnets (SPM in Figure 2.1). The nanoparticles generally used for biomedical applications and the particles used in our magnetic separation techniques span this size range of less than 30 nm and are thus all superparamagnetic. It may be important to note that in practice, the particle size regime where super-paramagnetism becomes relevant is found to vary among different materials so it might be different for iron oxide nanoparticles than it would be for other oxide nanoparticles.

In a colloidal magnetic fluid, each nanoparticle carrying a magnetic moment **m** can then be treated as a small thermally agitated magnet in the carrier liquid. Each particle in this fluid is randomly oriented in the absence of an applied magnetic field, and the fluid has no net magnetization. For ordinary field strengths, the tendency of the moments to align with the applied field is partially overcome by thermal agitation and as the magnitude of the applied field is increased, the particles become more and more aligned with the field direction. At higher field strengths, the particles may be fully aligned, with the magnetization achieving its saturation value. The usefulness of single domain magnetic nanoparticles lies in the fact that the particle's moment is about 10^5 times larger than that of transition or rare-earth metal ions. Therefore, when exposed to an external magnetic field, the whole colloidal solution behaves paramagnetically, with susceptibilities χ exceedingly high by similar order of magnitude, which is why saturation of magnetization in these particles can be reached in fields as relatively low as about .1 Tesla or 1 kGauss.

The superparamagnetic response of magnetic nanoparticles can be understood from some simple statistical mechanics considerations, assuming negligible particle-particle magnetic interaction. We know that in dilute superparamagnetic fluids, saturation is reached simply by rotation of all independent particle moments to align with the field direction to give a saturation magnetic moment. Starting with initial

conditions, we can consider a particle with moment of **m** initially directed at an angle θ to an applied field **H**. Assuming no anisotropic energy terms, the energy of this particle will be given by the well-known classical Zeeman energy term -mHCosθ[38]. If we have an assembly of particles at temperature T that have reached thermodynamic equilibrium with the field, there will be a Boltzmann's distribution of θ's over the particle assembly. The fraction of the total magnetization aligned by the field is calculated by averaging $Cos\theta$ over the Boltzmann distribution, which yields an integral expression

$$\bar{m} =< mCos\theta >= \frac{\int_0^\pi mCos\theta\, e^{\frac{mHCos\theta}{k_BT}} Sin\theta d\theta}{\int_0^\pi e^{\frac{mHCos\theta}{k_BT}} Sin\theta d\theta} \tag{2.4}$$

If we introduce a ratio between the energy of a particle in the applied magnetic field H and its thermal energy as $\alpha = \frac{mH}{k_BT}$, then the above expression may be written as

$$\bar{m} = \frac{\int_0^\pi mCos\theta\, e^{\alpha Cos\theta}\, dCos\theta}{\int_0^\pi e^{\alpha Cos\theta}\, dCos\theta} \tag{2.5}$$

$$\bar{m} = \frac{m}{\alpha} \frac{\int_{-\alpha}^{\alpha} xe^x\, dx}{\int_{-\alpha}^{\alpha} e^x\, dx} \tag{2.6}$$

where $x = \alpha Cos\theta$. When the integrations are carried out, the result is given by

$$\bar{m} = m\, L(\alpha) = m \left[\coth\alpha - \frac{1}{\alpha}\right] = Nm \left[\coth\left(\frac{mH}{k_BT}\right) - \frac{k_BT}{mH}\right] \tag{2.7}$$

which is commonly referred to as the Langevin function. N is the total number of magnetic nanoparticles in the sample, k_B is the Boltzmann's constant and T is the temperature. Once could also decide to write the moment of a particle as **m**= n μ_B where n is the number of Bohr magnetons in a representative particle and μ_B is the Bohr magneton.

A Langevin function is traditionally used to fit the curve of magnetization or magnetic moment vs. applied field (**M** vs. **H** curve) for superparamagnetic nanoparticles. The fit allows us to extract information about the saturation mass magnetization of the particle's material and the magnetic moment per average particle. A plot of the Langevin function for different magnetization and particle moment values is shown in Figure 2.3.

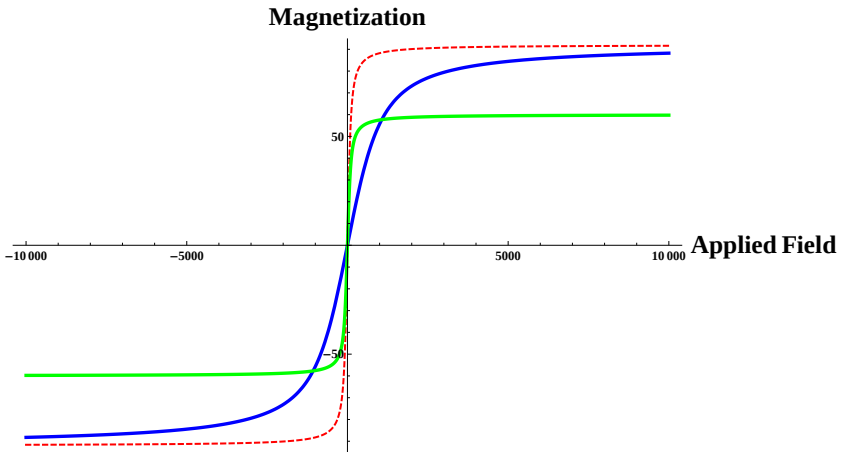

Figure 2.3: A plot of the Langevin function allows us to distinguish between samples differing in their particle moments and magnetizations. Nanoparticle samples that differ in their saturation magnetization values are represented by dashed red and green curves, where dashed red has a higher magnetization. Similarly, samples with the same magnetization but differing in their particle moments are represented by dashed red and solid blue curves, where blue represents a sample with a smaller value of magnetic moment per particle.

The magnetization of the sample may be calculated by dividing the total moment of the sample by the volume of suspended magnetic material. Sometimes if a magnetic nanoparticle exhibits a core shell structure, made of magnetically differentiable materials like magnetite (Fe_3O_4) and maghemite (γ-Fe_2O_3), one can roughly estimate the core shell dimensions using information extracted from the Langevin fitting. However, when working with superparamagnetic nanoparticles, one needs to be careful of the possibility of significant variation in values of saturation magnetization between individual particles and bulk, leading to erroneous conclusions.

2.3 Theory of magnetic separation

A single domain, isolated magnetic particle of total magnetic moment $\mathbf{m}$ in an inhomogeneous applied field $\mathbf{H}_0$ experiences a magnetic force:

$$\mathbf{F}_m = (\mathbf{m} \bullet \nabla)\mathbf{H}_0 \tag{2.8}$$

where ∇ is the gradient operator evaluated at the location of the particle [39]. In the case of a magnetic nanoparticle suspended in a very weakly diamagnetic or paramagnetic medium such as toluene or water, the total moment on the particle can be written as $\mathbf{m} = \mathrm{V}_m\ \mathbf{M}$, where V_m is the magnetic volume of the particle and $\mathbf{M}$ is its

volumetric magnetization. Furthermore, provided there are no time-varying electric fields of currents in the medium, we can apply Maxwell's equation $\nabla\times\ \mathbf{H}_0 = 0$ to the mathematical identity:

$$(\mathbf{m} \bullet \nabla)\mathbf{H_0} = \nabla(\mathbf{m} \bullet \mathbf{H_0}) - \mathbf{H_0} \bullet \nabla\mathbf{m} - \mathbf{m} \times (\nabla \times \mathbf{H_0}) - \mathbf{H_0} \times (\nabla \times \mathbf{m}) \quad (2.9)$$

For constant $\mathbf{m}$ this simplifies to:

$$(m \bullet \nabla)\mathbf{H_0} = \nabla(\mathbf{m} \bullet \mathbf{H_0}) - \mathbf{m} \times (\nabla \times \mathbf{H_0}) \quad (2.10)$$

When there is no flow of electric current, $\nabla \times \mathbf{H}_0$ is identically zero, and therefore for a dipole of fixed moment $\mathbf{m}$ the force can be written as

$$\mathbf{F}_m = \nabla(\mathbf{m} \bullet \mathbf{H}_0) \quad (2.11)$$

This relation summarizes the force on a single particle of fixed moment as a function of its orientation and position in the applied field H_0. Also, this relation shows that a spatially varying magnetic field is required to create a magnetic force, which is the only parameter controlled by the magnet design; the other term depends on the size and material properties of the particles.

For a particle in solution of viscosity η, this force may be opposed by a resulting Stokes' drag force of

$$F_d = -3\pi\eta d_p \mathbf{v_p} \quad (2.12)$$

where d_p is the effective particle diameter in solution, and v_p is its velocity. For

$$\mathbf{F_d} + \mathbf{F_m} = \mathbf{0} \quad (2.13)$$

the particle achieves a steady state v_p which, for sufficiently large $\mathbf{m}$ and large gradient in field, may be sizeable enough to allow for separation of the particle in a magnetic separation process. It is important to note that the largest magnetostatic forces on the particles will be at the region closest to the magnet. This is because the magnetic field is highest adjacent to the magnets, causing greatest magnetization of the particles and thus exerting the greatest magnetic force. It is not surprising then that particles will move towards the magnet not because of gravitational settling (since gravity is a much smaller force on the particle), but primarily due to magnetic causes.

In addition to a single particle interaction with the applied field, we must also consider the possibility of inter-particle interactions in the presence of an applied field, so far ignored. For two magnetic nanoparticles, the dipole-dipole energy [39] can be calculated by

$$U_{dd} = \frac{\pi \mu_0 M^2 d_m^6}{72(d_m + 2\delta)^3} \tag{2.14}$$

where the particles have magnetization values of M, magnetic diameter d_m and non-magnetic coating thickness δ. Note that the magnetic diameter d_m may be significantly different from the effective particle diameter in solution d_p, as the particles may have a sizeable portion that is not magnetic as a result of surface effects or more simply due to a surfactant coating.

The dipole-dipole interaction energy between particles U_{dd} and the thermal energy $k_B T$ come to be around similar values for magnetic nanoparticles. These energies compete to determine whether particles will aggregate or flow freely exhibiting Brownian motion in the magnetic colloid. The tendency for superparamagnetic particles to aggregate is expected to increase with particle size, in part due to greater magnetization in larger particles caused by larger magnetic susceptibilities [40]. In addition, Begin-Colin and co-workers indicate that smaller sizes of iron oxide crystals are enriched in the less magnetic iron oxide called maghemite (γ-Fe_2O_3) as opposed to the more magnetic magnetite (Fe_3O_4) which may decrease their magnetic moment and contribute to minimal aggregation due to reduced response to external fields [41].

Once the field is removed, particle interactions immediately diminish and the observed aggregate structures dissolve into the suspension. This is also an essential difference between dispersion of superparamagnetic and ferromagnetic particles: in the case of particles with a permanent dipole (ferromagnetic particles), aggregates would still be observed in the absence of magnetic field due to the remanent dipole-dipole interaction. The reversible field-induced aggregation in superparamagnetic nanoparticles helps to dramatically enhance magnetophoresis, which is the movement of particles in an applied field gradient. According to Camacho et al. [40], initially the magnetophoretic velocity of the particles is very slow, but large chain-like aggregates are rapidly formed, moving fast and colliding with other aggregates to produce even larger structures at faster velocity. This increase in magnetophoretic velocity increases the throughput of methods that employ such reversible aggregation by orders of magnitude.

2.4 Theory of small angle x-ray scattering

Small angle x-ray scattering (SAXS) is a widely used and well understood wave-diffraction method for studying the structure and ordering of matter. This method of elastic scattering is used in various branches of science and technology, including condensed matter phyics, biophysics, polymer science, and metallurgy. In small angle x-ray diffraction experiments, a primary beam of x-rays influences a studied object, and the scattering pattern is analyzed in the range of 2θ from 0 to around 5 degrees, where 2θ is the angle between the source and the detector as shown in Figure 2.4. This analysis provides information on the structure of a substance with a spatial

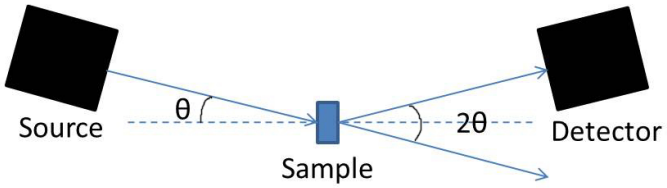

Figure 2.4: Schematic of x-ray scattering showing angle 2θ between the source beam and the scattered beam received by the detector.

resolution from 10 Å to thousands of Angstroms. Below, we review the basic theory of stationary scattering result with no time dependence in the elastic scattering case where the wavelength of the x-ray and magnitude of the wavevector $\mid \mathbf{k} \mid = \frac{2\pi}{\lambda}$ does not change upon scattering. We describe the form factor for spherical particles and obtain an expression for scattering intensity observed in all our experimental plots. Further information can be found in any of the various texts on small angle X-ray scattering [42, 43, 44].

X-ray scattering occurs when particles differing in electron density from their surrounding matrix are irradiated with monochromatic x-rays, modeled as a plane wave $\psi = e^{i(\mathbf{k}\cdot\mathbf{r}-\omega t)}$ where $\mathbf{k}$ is the wave vector, $\mathbf{r}$ is the path difference between the wave and a scattering origin, and ω is the angular frequency of the x-ray. If the final wavevector $\mathbf{k}_f$ is deflected at an angle 2θ from the initial wavevector $\mathbf{k}_i$, assume $\mathbf{Q}$ is the scattering vector given by the difference between the final and inital wavevectors, shown in Figure 2.5 and defined by:

$$\mathbf{Q} = \mathbf{k}_f - \mathbf{k}_i \qquad and \qquad \mathbf{Q} = \frac{4\pi}{\lambda} sin\theta \tag{2.15}$$

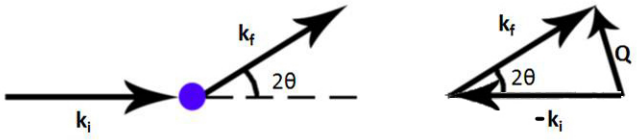

Figure 2.5: Schematic of x-ray scattering showing initial and final wavevectors $\mathbf{k}_i$ and $\mathbf{k}_f$ and the scattering vector $\mathbf{Q}$

Unlike the incident beam which is collimated, the intensity of the outgoing wave per unit area will fall dramatically after scattering. Due to the phase change introduced from our nanoparticle sample at distance r, the scattered wave will take the general form:

$$\psi_f = \psi_0 G(\lambda, \theta) \frac{e^{i\mathbf{k}\cdot\mathbf{r}}}{r} \tag{2.16}$$

where ψ_0 ensures that the rate of scattering is proportional to the incident flux, and the function G(λ, θ) tells us about the chances that a wave of given wavelength λ is deflected in a certain direction θ from the incident wave direction. For any real sample radiated with a beam of x-rays, the challenge for finding the pattern that will result is summing up all the n scattered waves from each individual scattering event to produce a complete scattered intensity profile. The amplitude of the resulting wave in the direction of $\mathbf{Q}$, notated as F$(\mathbf{Q})$, gives the diffraction pattern in Q-space detected in experiments:

$$F(\mathbf{Q}) = \sum_{0}^{n} e^{-i\mathbf{Q}\cdot\mathbf{r}_n} \tag{2.17}$$

where F$(\mathbf{Q})$ is the Fourier transform of the electron density fluctuations within the object depending on the form of particles. Typically in the study of crystal diffraction, the scattering amplitude F$(\mathbf{Q})$ is given by the product of the form factor f$(\mathbf{Q})$ and the structure factor S$(\mathbf{Q})$. The form factor is a measure of the particle shape and composition, while the structure factor which is a measure of the arrangement of scattering sources. In our case, the structure factor will not contribute to the scattering amplitude because our samples are magnetic particle colloids randomly suspended in medium and not arranged in any regular order. Therefore, the scattering intensity I$(\mathbf{Q})$, which is the square of the scattering amplitude, depends purely on the form factor squared.

$$F(\mathbf{Q}) = f(\mathbf{Q})S(\mathbf{Q}) \tag{2.18}$$

$$I(\mathbf{Q}) \propto |F(\mathbf{Q})|^2 \propto |f(\mathbf{Q})|^2 \tag{2.19}$$

To understand what sets the F(**Q**) and how it relates to electron density in a sample, we can look at the atomic cross section of the material, following the method of Windsor [45]. If a sample contains N atoms of type i, each with atomic cross sections $d\sigma/d\Omega_i$, atomic density d_i and atomic weight A_i, then the cross section for some macroscopic portion of sample is given by

$$dE/d\Omega = \sum_{0}^{n} \left(\frac{N_A d_i}{A_i} \right) d\sigma/d\Omega_i \tag{2.20}$$

where N_A is Avogadro's number. The atomic cross section can be thought of as the total amount of material in a given volume that will scatter the incoming beam. This quantity, integrated over all $d\Omega$ and multiplied by 4π will give the exact fraction of the beam scatter by the sample. The uneven distribution of particles in space leads to a collection of scattered phases within the sample. For each distinct phase j, it is possible to define a scattering length density, essentially an average scattering length density ρ_j in terms of a bound coherent scattering length b_j:

$$\rho_j = \frac{N_A d_i b_j}{A_i} \tag{2.21}$$

If the sample is assumed to be in a medium of scattering length density ρ_0 such that the difference of electron density is $\Delta\rho{=}\rho - \rho_0$, the macroscopic cross section in Equation 2.20 gives rise to the form factor due to the particle shape and composition integrated over the particle volume:

$$f(Q) = \frac{1}{V} \int_V \Delta\rho(r) e^{i\mathbf{Q}\cdot\mathbf{r}} dr \tag{2.22}$$

There are many common particle structures for which the form factors have been derived. One of the simplest systems, a hard sphere, has been derived below since it is the structure of most relevance for our nanoparticle structure. Using an

approximation and substituting it in Equation 2.22:

$$\langle e^{i\mathbf{Q}\cdot\mathbf{r}} \rangle = \frac{sin(\mathbf{Q}\cdot\mathbf{r})}{\mathbf{Q}\cdot\mathbf{r}} \tag{2.23}$$

$$|f(\mathbf{Q})|^2 = \frac{1}{V}|\Delta\rho|^2 \left| \int_0^R \frac{sin(\mathbf{Q}\cdot\mathbf{r})}{\mathbf{Q}\cdot\mathbf{r}} dr \right|^2 \tag{2.24}$$

$$|f(\mathbf{Q})|^2 = \frac{1}{V}|\Delta\rho|^2 \left| \frac{3}{(\mathbf{Q}\cdot\mathbf{R})^3} [sin(\mathbf{Q}\cdot\mathbf{R}) - \mathbf{Q}\cdot\mathbf{R}cos(\mathbf{Q}\cdot\mathbf{R})] \right|^2 \tag{2.25}$$

$$|f(\mathbf{Q})|^2 = |\Delta\rho|^2 \left| \frac{4\pi}{(\mathbf{Q})^3} \left(sin\left[\frac{\mathbf{Q}\cdot\mathbf{D}}{2}\right] - \frac{\mathbf{Q}\cdot\mathbf{D}}{2} cos\left[\frac{\mathbf{Q}\cdot\mathbf{D}}{2}\right] \right) \right|^2 \tag{2.26}$$

where R is the radius of a nanoparticle in the sample and D is the diameter. A theoretical plot of this scattering intensity with respect to **Q** for two different sizes of perfectly spherical particles is given in Figure 2.6. The pronounced minima seen in the figure are rare for experimental results due to a distribution of radii and imperfectly shaped particles.

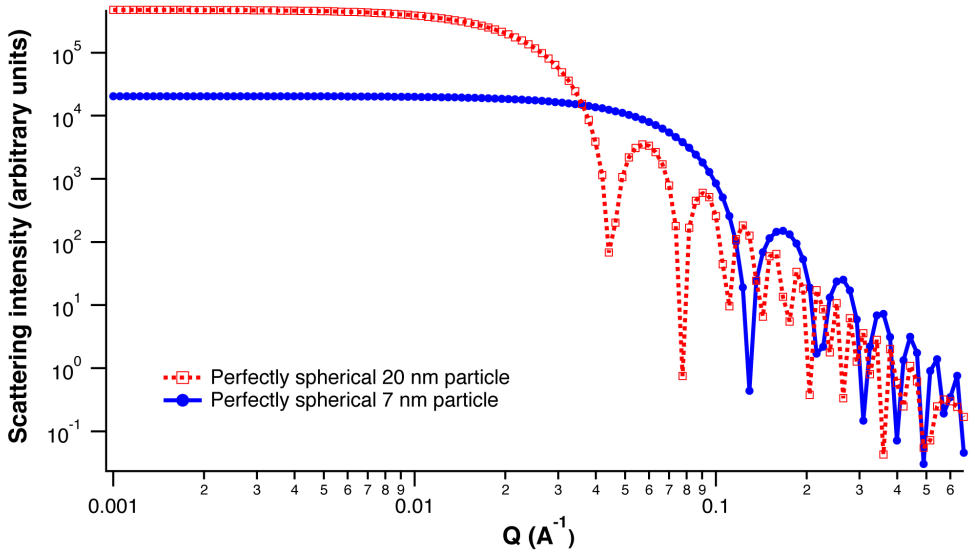

Figure 2.6: Theoretical plot of x-ray scattering intensity from perfectly spherical 20 nm and 7 nm particles as modeled by Equation 2.26.

Typically when we are dealing with a sample of large number of nanoparticles, we assume that these particles have a distribution of particle sizes. Let us assume these sizes are distributed according to the Γ-distribution function P(D, D_0, σ) represented by Equation 2.27 where D_0 is the average diameter of particles, and σ is the normalized variance:

$$P(D, D_0, \sigma) = \frac{1}{\Gamma(1/\sigma^2)} \left[\frac{1}{\sigma^2 D_0}\right]^{(1/\sigma^2)} D^{-1+1/\sigma^2} exp\left[-\frac{D}{\sigma^2 D_0}\right] \tag{2.27}$$

Then the final expression for scattering intensity is $I(\vec{Q}) = |F(\mathbf{Q}, D_0, \sigma)|^2$ given by Equation 2.28:

$$= |\Delta\rho|^2 \left| \frac{4\pi}{(\mathbf{Q})^3} \left(sin\left[\frac{\mathbf{Q}\cdot\mathbf{D}}{2}\right] - \frac{\mathbf{Q}\cdot\mathbf{D}}{2} cos\left[\frac{\mathbf{Q}\cdot\mathbf{D}}{2}\right] \right) \right|^2 \times P(D, D_0, \sigma) \frac{D_0^3}{D^3}\, dD \quad (2.28)$$

Therefore, when SAXS measurements of nanoparticles are carried out in the transmission geometry, the scattering intensity can be modeled by Equation 2.28. If we assume that the particle sizes are arranged according to a lognormal distribution function, which is another size distribution function commonly used in the analysis of nanoparticle sizes, we can simply replace the gamma distribution function with the lognormal distribution in Equation 2.28. A theoretical plot is shown below in Figure 2.7 depicting scattering intensity vs. angle (converted from $\mathbf{Q}$ using Equation 2.15) from a lognormal distribution of Fe_3O_4 spheres with average diameters of 7 nm and 20 nm and dispersion of 10%, each suspended in a toluene medium. The sharpness of minima helps to characterize the size distribution of particles. Notice that the sharp minima associated with perfect spheres is now much less pronounced due to the distribution of sizes and the liquid medium.

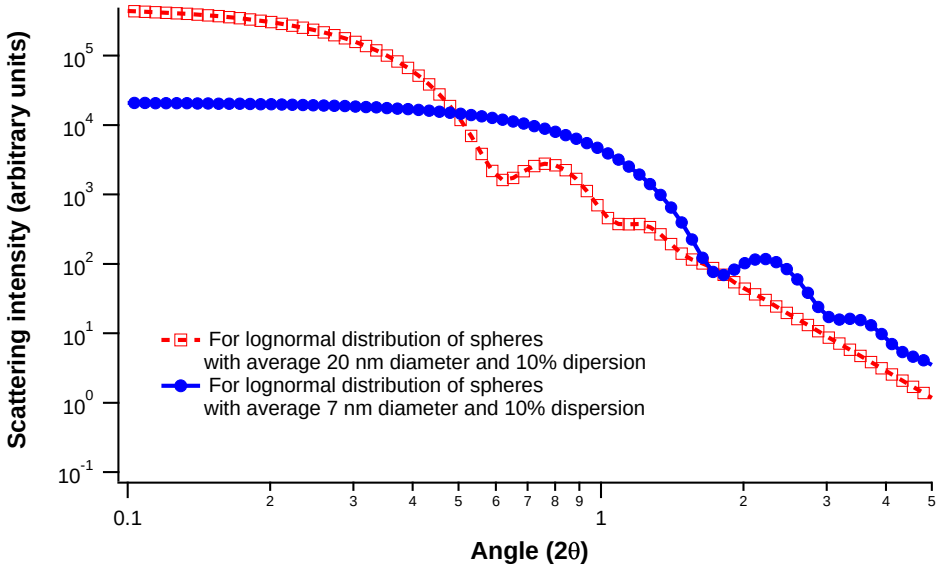

Figure 2.7: Theoretical plot of x-ray scattering intensity from a lognormal distribution of spheres with average diameters 7 and 20 nm and 10% dispersion.

Chapter 3

The Halbach Array: Design, Construction and Characterization

We have investigated the modeling, design, construction and characterization of a linear Halbach arrangement of permanent magnets. This magnet array has been shown to exert small spatially uniform magnetic field while at the same time obtaining a large magnetic gradient, within the physical constraints imposed by Maxwell's magnetostatic equations. In the sections below, we explain in detail the modeling of the magnet array behavior using finite element modeling, along with the designing of the array and associated flow channels using specialized CAD software. We then outline the actual construction of the linear Halbach array before investigating its field measurements, the array behavior and its implications for magnetic separation.

3.1 Finite Element Modeling

As described earlier, we hypothesized that the low flux side of a linear Halbach array could provide characteristics desirable for magnetic separation of nanoparticles, such as high magnetic field gradient and low field. To develop the concept further, we used finite element modeling to simulate the magnetic field and gradient profiles across a linear Halbach array model. The modeling was performed using FEMMView (Finite Element Method Magnetics) software [46] that solves two dimensional planar electromagnetic problems and in our case, linear magnetostatic problems using

differential equations and the standard Maxwell's equations [36]:

$$\nabla \times \mathbf{H} = \mathbf{J} = 0 \tag{3.1}$$

$$\mathbf{B} = \mu_0(\mathbf{H} + \mathbf{M}) \tag{3.2}$$

$$\nabla \bullet \mathbf{B} = 0 \tag{3.3}$$

where $\mathbf{J}$ is the current density which is zero in our case and other symbols have already been defined earlier. These equations hold true in vacuum as well as in materials (air and liquid), and for electromagnetism and permanent magnets (magnetization $\mathbf{M} \neq 0$). Since it is typically very difficult to get closed-form solutions for all but the simplest geometries, finite elements uses the concept of breaking down the problem into a large discrete number of simple triangular regions over which the "true solution" for the desired potential is approximated by a very simple function. This discretization essentially forms a large but easy linear algebra problem solved by minimizing the error between the exact differential equation and the approximate differential equation as written in terms of linear trial functions.

For our model, 47 blocks were arranged linearly and each block was assigned the property of uniformly magnetized Neodymium Iron Boron (NdFeB) magnets, which are a class of commonly found permanent magnets that can be made into various different sizes and shapes and can be magnetized with very specific magnetization directions. The magnetization direction of successive magnets in the array differed by 90 degrees in a regular pattern. Figure 3.1 shows magnetic field lines from the linear magnet array model that was created using FEMMView. Although we designed the model starting out with all magnets at the same level, measurement of the normal B field from the physical array constructed using this model suggested that every other magnet (with their magnetizations directions horizontal) had shifted 5% from the original structure. The model was then adjusted to account for such a shift, with the final model shown in the inset of Figure 3.1 The calculated magnetic flux density data were extracted from the modeling software and imported into the graphing and data analysis software package Igor Pro.

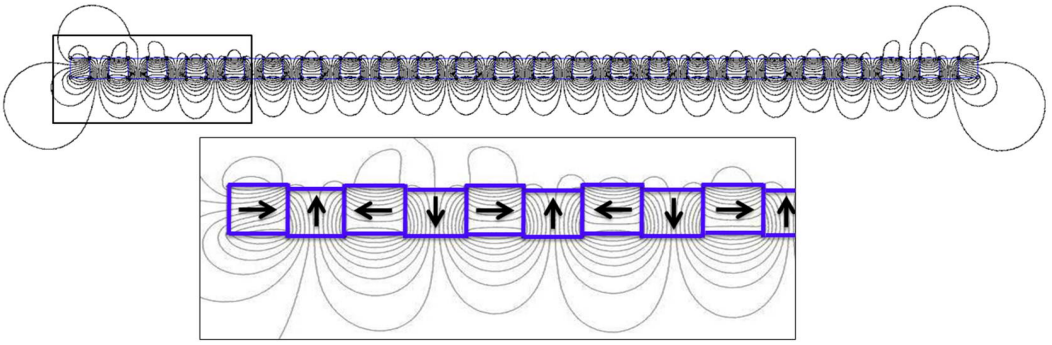

Figure 3.1: (a) Finite element method model of the Halbach array. (b) Magnified Halbach array profile to show magnetization orientation of successive magnets.

3.2 Computer aided designs of magnet array and flow channels

Computer-aided designs (CAD) were made using Solidworks Premium 2013, a 3D mechanical solid modeler CAD program that allowed to easily create models and assemblies of parts. Designs of the magnet array were created in SolidWorks by our collaborators in Cleveland Clinic's Lerner Research Institute before the actual construction of the device. They also designed an associated toluene-compatible flow channel with layers of different materials that could be sandwiched together and held tightly by screws to prevent leaks in the system. This channel contains a Viton rubber gasket sandwiched between a stainless steel base and a borosilicate glass top plate. All three of these materials were chosen for excellent corrosion resistance to toluene and can also be used for aqueous suspension separations. A Plexiglas cover (design shown in Appendix A) sits on top and holds down all the components tightly using 22 large screws to prevent leaks while also allowing to view separation progress during liquid flow. This assembly with different component layers including the magnet array is shown in Figure 3.2. Based on this design, we describe the materials and dimensions used in the actual construction of this channel in Section 3.3.

We later designed a second water-compatible Plexiglas channel (design in Appendix A), shown in Figure 3.3 consisting of thinner medical grade silicone gasket sandwiched between a transparent Plexiglas top plate and a stainless steel bottom plate. The lower surface of the bottom plate was designed to be extremely thin, about 0.13 cm, allowing us to access higher fields and gradients closer to the array when particles flow on top of this plate. These materials were chosen for water

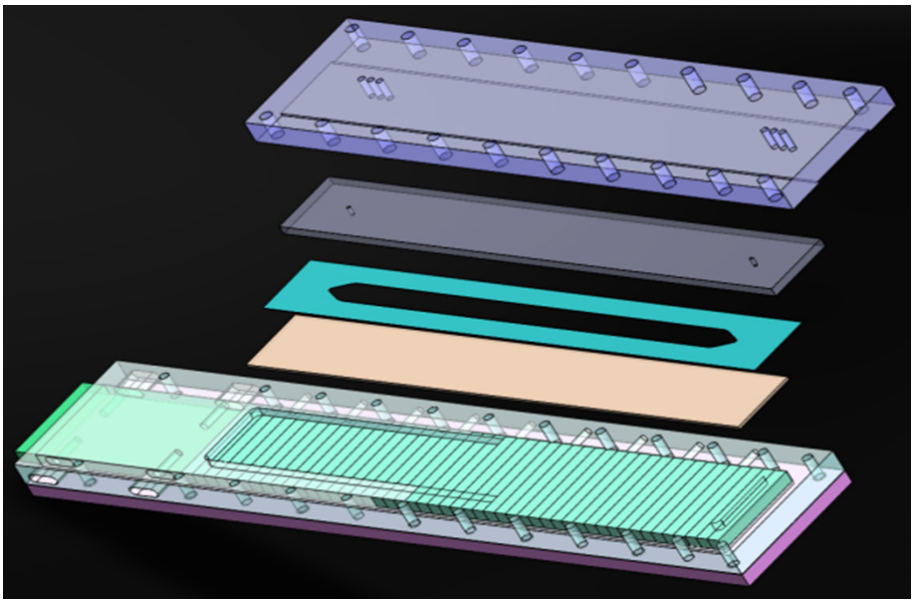

Figure 3.2: Array-channel assembly design with toluene-compatible glass channel.

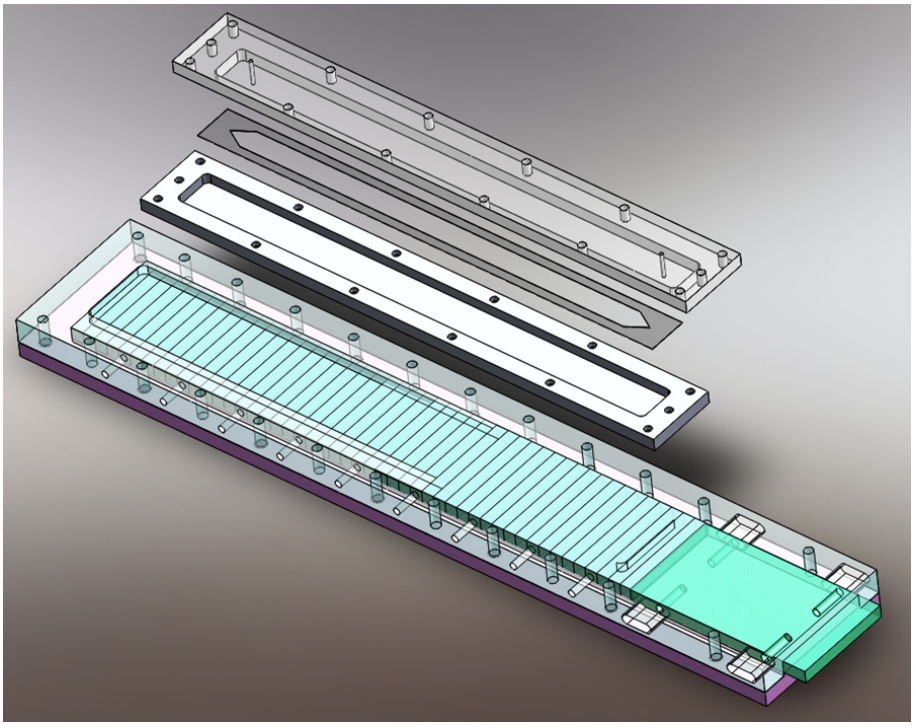

Figure 3.3: Array-channel assembly design with water-compatible Plexiglas channel.

compatibility, the ability to view separation progress during liquid flow, and resistance to cracking under pressure. These considerations limited our selection of top plates to a few transparent machinable plastics, among which all of them corroded in contact with toluene or organic solvents. Therefore, this new channel is only water-compatible and cannot be used with toluene suspensions. However, it is lighter, more portable, and can easily be lifted to change array-channel distance during a separation without any leaks and without having to unscrew the 22 large screws that held the toluene-compatible channel.

3.3 Device construction

As shown in Figure 3.4, an inverted Halbach array has been constructed with 47 nickel-plated Nd-Fe-B magnets (42 MGOe energy product, K&J Magnetics, Inc), each with dimensions of 0.64 cm (width) 0.64 cm (height) 5.08 cm (length) and magnetized through a 0.64 cm dimension. Across the array, the magnetization direction of each magnet is rotated by 90 degrees. The magnets are held in place with set screws and an aluminum frame, but there are height variations from magnet to magnet of around 5%, which have been accounted for in our FEMM model as well. The array dimensions have been chosen to make use of readily obtainable magnets and other materials.

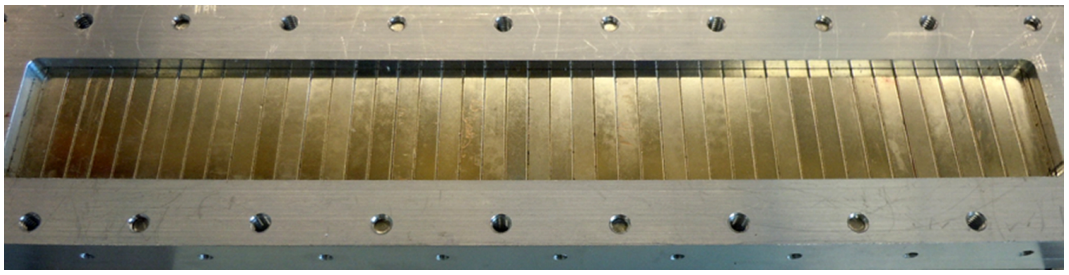

Figure 3.4: The constructed linear Halbach magnet array with 47 NdFeB magnets held together by set screws and an aluminum frame.

Figure 3.5 depicts banding patterns due to toluene-based nanoparticle aggregation in our first flow channel. The channel has dimensions of 23.3 cm (length) 1.27 cm (width) 0.025 cm (thickness), with an inlet to outlet distance of 22.9 cm. FEP Teflon tubing (0.08 cm inner diameter) has been used for the inlet and outlet, with magnetic suspensions injected or withdrawn using a syringe pump (Harvard Apparatus Syringe Pump 11 Elite). Additional stainless steel spacer plates can be used to adjust the distance of the channel from the array.

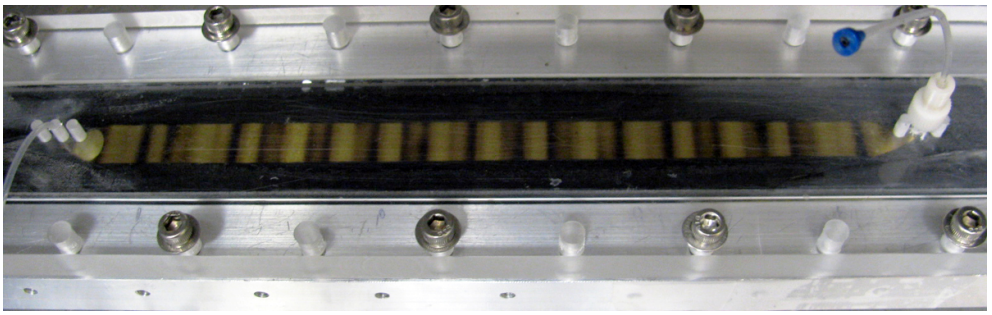

Figure 3.5: The toluene-compatible glass channel on top of the Halbach array during a separation process shows aggregation of nanoparticles at distinct locations above the array where gradient of the field is highest.

Our second flow channel is depicted in Figure 3.6, with similar banding patterns seen in the case of water-based suspensions.

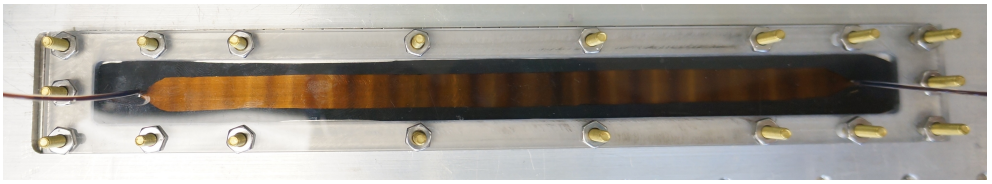

Figure 3.6: The water-compatible glass channel during a similar separation process. This design is lighter, more portable and easily allows adjusting distances between the array and channel, even during separations.

3.4 Characterization of constructed Halbach array

The validity of the finite element modeling, described earlier in section 3.1, has been tested by measuring the magnetic field normal to the magnet assembly with a Hall effect gaussmeter (Lakeshore 410 gaussmeter) for several distances above the array parallel to the surface as shown in Figure 3.7. Through the central portion of the array, there is relatively good agreement between the measured and modeled values of the normal component of **B**.

Figure 3.8 shows the data for the normal component of the field measured at a distance of 0.3 cm from the magnet array surface (dashed blue), a distance commonly used for many of our nanoparticle separations where the average peak field value has been found to be approximately 50 mT. Also shown in the figure are the results of finite element method calculations performed with FEMMView software, indicating the predicted field value(solid red). The gradient(green) has an average value of 32 T/m at that height.

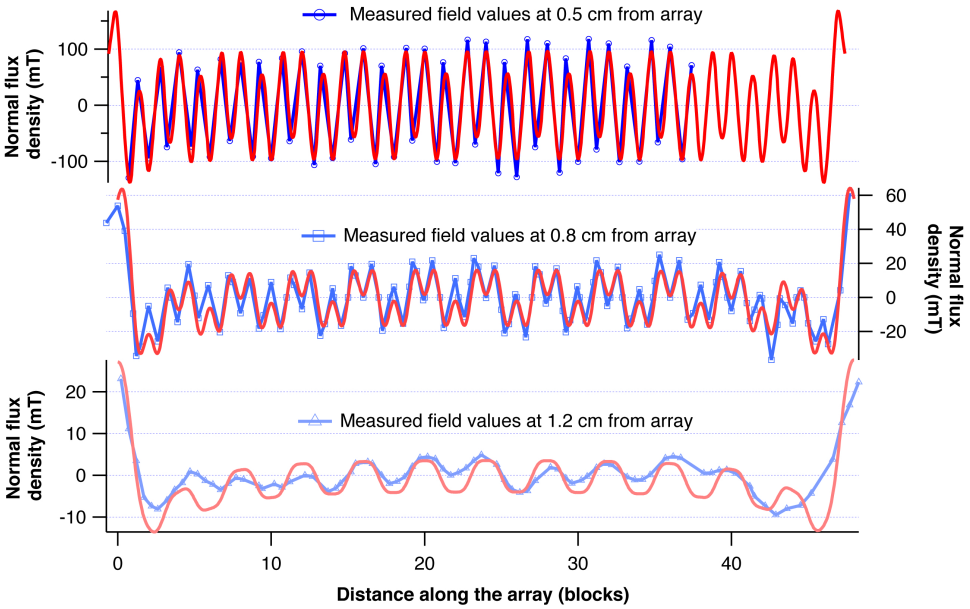

Figure 3.7: Comparison of the normal component of the **B** field along the length of the magnet array at different distances away from the array (each block is 0.64 cm), as modeled with FEMMView (red) or measured with a gaussmeter probe (blue).

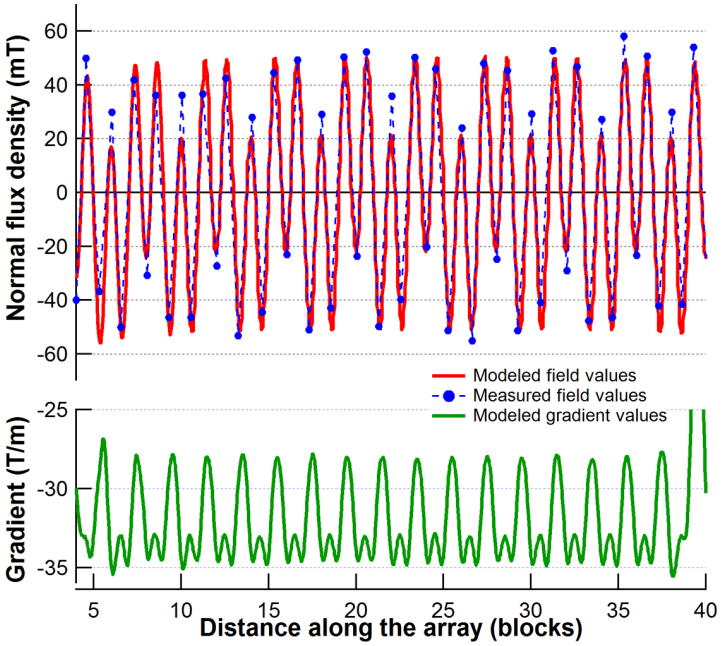

Figure 3.8: (a) Plot of the normal component of the **B** field along the length of the magnet array at a distance 0.3 cm from the low flux side of the array (each block is 0.64 cm), as modeled with FEMMView (solid red) or measured with a gaussmeter probe (dashed blue). (b) Plot of the corresponding gradient of the field from FEMMView calculations.

The good agreement between modeling and measurement results at multiple distances from the array provides evidence that the model is faithful to actual device characteristics, allowing us to use the finite element model for further pertinent calculations. The field data from the model plotted in Figure 3.9 shows slight variations but in general, good uniformity in **B** field along the entire horizontal distance of the array. At distances very close to the array, there is much greater variation in the **B** field but the array still maintains uniformity in peak field values. However, at the two ends of the array (the last 2.5 cm on each side), fringe effects occur making the field highly irregular (not shown in figure) but for our separations, the flow channel location and its width and length have been chosen to be in the uniform field region to avoid these end effects.

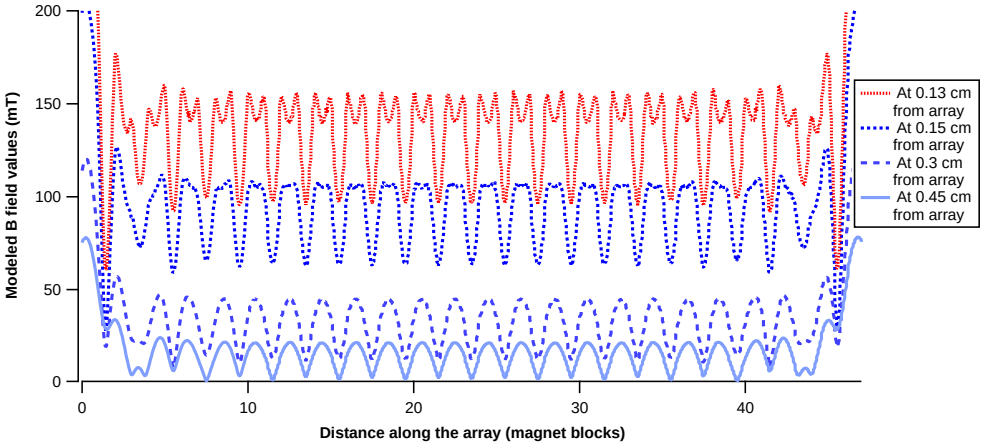

Figure 3.9: Plot of the **B** field along the length of the magnet array at four different distances relevant for separation away from the array, as modeled with FEMMView. The highest field values are reached in the new Plexiglas channel when used without spacers, while the three lower field values are reached with the old glass channel when 1, 2 and 3 spacers, each of thickness 0.15 cm rest underneath.

FEMMView modeling results have also confirmed the utility of our approach in using the low flux side of the Halbach array, in comparison to the expected behavior for a single magnet or the high flux side of the array. We can see in Figure 3.10 that the gradients for low flux side of the Halbach array are significantly higher for the same values of field - which supports the central premise of this separation approach, namely that a high field gradient ∼30 T/m can be achieved in low field ∼50 mT. In addition, the array provides a large region for separation of nanoparticle suspensions as opposed to a very small region above a single magnet.

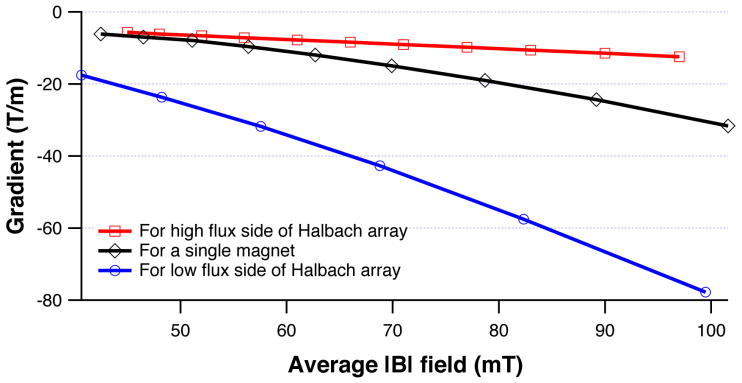

Figure 3.10: Comparison of field gradient as a function of average **B** field for the high and low flux sides of the Halbach array and for a single magnet shows the utility of using the low flux side.

The significantly higher gradient at the low flux side for the same medium and set of particles increases the flow rate of the particles linearly as given by modification of Eqn 2.13 on page 15 into

$$v_p = \frac{\nabla(\mathbf{m} \bullet \mathbf{B})}{3\pi\eta d_p} \tag{3.4}$$

Based on the field values we are using, a three to sixfold higher gradient makes each separation 3 to 6 times faster. Therefore our idea of a high throughput separation process of magnetic particles is best served by using the low flux side of the array.

When we are using the array in the low flux side, the average **B** field and field gradient of the array both get changed just by changing the distance of the channel from the array surface. Figure 3.11 presents the values of magnetic field and gradient along the channel as a function of the array-channel distance calculated using our model. Consider, for example, a decrease in the distance between the array and the channel. This increases the field gradient and thus increases the force on a suspension of nanoparticles (Eqn 2.8), making the separation faster.

3.5 Implications for magnetic separation

Next, we develop a schematic of separation process and particle behavior in a channel placed at different distance from the Halbach array using the concepts of magnetic force and dipole-dipole energy and using a number of generalized assumptions. First, we can assume that the magnetic field generated by the Halbach magnet array is uniform throughout the horizontal distance of the array and inversely proportional

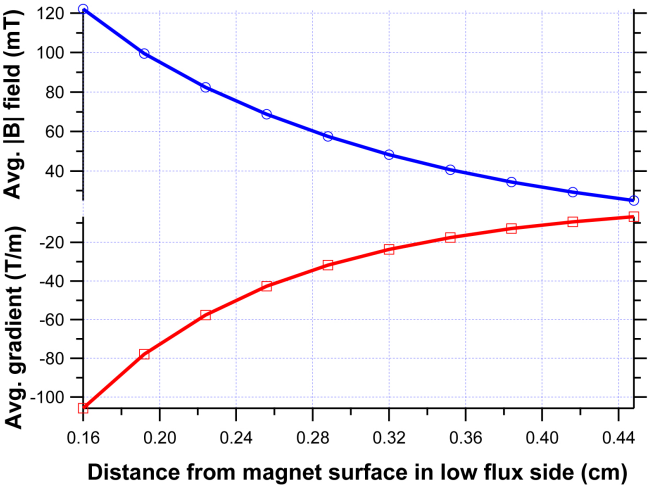

Figure 3.11: Plot of the (a) averaged **B** field and (b) gradient of **B** in the direction perpendicular to the surface of the magnet array as a function of distance above the array in the low flux side.

to distance from the array (supposedly located right below the schematic) as shown in Figure 3.12, where the field strength is higher in the bottom strip than in the top strip. The channel full of particles can be situated at different distances from the magnet array. Noting the directly proportional relation between U_{dd} and magnetization M in Equation 2.14, we can infer that U_{dd} between particles will be greatest at a region closest to the magnet array where particles experience the greatest magnetic fields and get most magnetized.

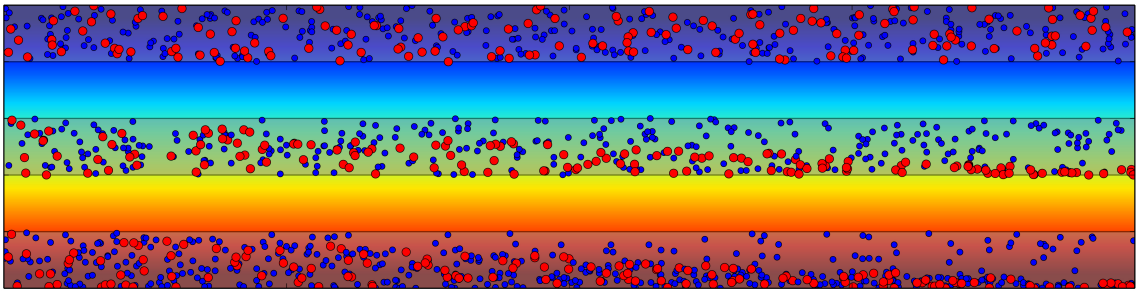

Figure 3.12: Schematic of separation showing field and particle behavior at different distances away from the array: the bottom strip represents highest field and gradient values, both of which decline as we move up and away from the array. Sorting close to the array near the bottom leads to maximum aggregation of particles while sorting far away from the array leads to minimum aggregation. Somewhere in between, we expect an optimum distance where aggregation of more magnetic particles and random flow of less magnetic particles can be expected.

Next, we can make the assumption that magnetization of particles scales with size, which is a reasonable assumption to make for particle suspensions manufactured using the same synthesis process [40]. For a mixed suspension of large (red) and small

(blue) particles flowing in the channel in moderate (middle strip) to high magnetic fields (bottom strip), U_{dd} for larger particles can become much greater than thermal fluctuations of order k_BT. This may result in a distribution of clustered and chained large nanoparticles at the bottom of the channel. On the contrary, for small particles, thermal energy dominates the dipole-dipole interaction energy and prevents the particles from clustering to each other, letting them flow freely through the fluid.

There are some trade-offs to balance here in terms of what particles we would like to isolate in the post-sort filtrate and post-sort residues and the quality (in uniformity) of these filtrates and residues. This balance depends critically upon the distance of the channel from the magnet array since this distance not only alters the gradient and magnetic force experienced by the particles as described before, but also the magnetization and dipole-dipole interactions between individual particles due to change in field.

Doing a separation too close to the array (bottom strip) strengthens the dipole-dipole interactions between all particles and brings about the complication and undesirable effect of particle aggregates interacting with both large and small particles. This traps even some smaller particles in the residue instead of letting them flow freely into the filtrate. This might produce a good filtrate by letting only small particles flow freely but will surely reduce the uniformity of the residue. Similarly, placing the channel far away from the array (top strip) reduces the dipole-dipole interactions and brings about another undesirable effect of even large particles not being trapped in the array as residue, and just flowing through to the filtrate instead. In this case, the residue might contain only some larger particles that clumped, making it more uniform but the quality of the filtrate is compromised.

Another schematic, Figure 3.13 (c), shows explicitly the nanoparticle suspension flow and the effect of locating a channel in an ideal sorting situation, with large particles trapped in periodic locations along the array where both gradient and field are greatest. However, even when the optimal distance has been calculated and used, some of our assumptions about the particles can go awry, leading to sub-optimal sorting conditions. Say for example, that the assumption of particle magnetization scaling with size is defective, meaning that there are some large particles with magnetization comparable to or weaker than the smaller particles and that there are some small particles with very high magnetization. In this case, the small particles can potentially start interacting with a cluster of large chained nanoparticles if the dipole-dipole energy between the particle-cluster combination exceeds the thermal

energy. Different-sized nanoparticles could be entangled or trapped inside this cluster as it forms, making the separation process more challenging. Similarly, there might be larger particles with smaller values of magnetization that never get trapped at the base but instead, flow out along with the smaller particles even when we are at an optimum distance. The schematic in Figure 3.13 (d), shows the result of these various complications that could occur when working with particles originating from mixtures synthesized at different times.

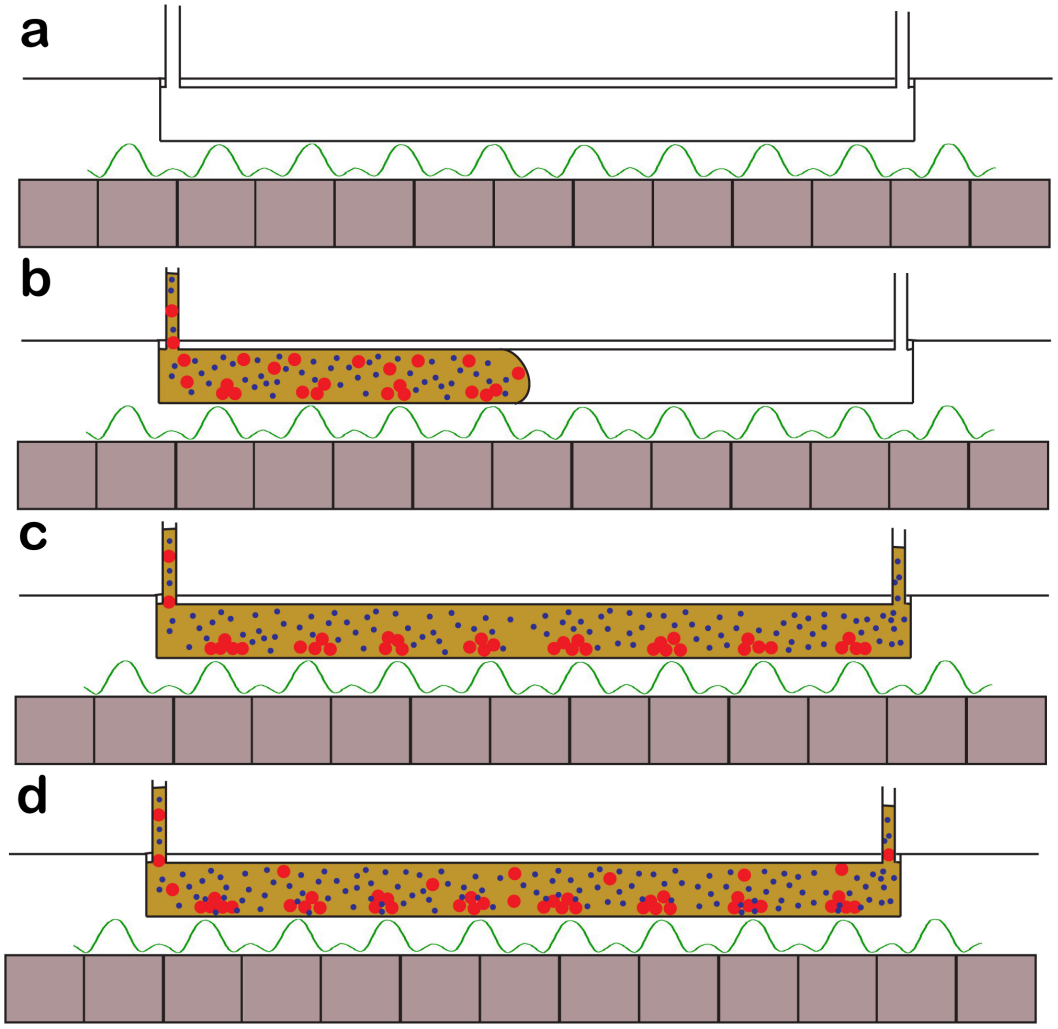

Figure 3.13: Schematic of separation at an optimal distance and complications that could arise: (a) Placing the channel at an optimal distance. (b) Flowing a mixed suspension with large and small nanoparticles into the channel from an inlet. (c) Ideal sort behavior with smaller particles flowing out of the outlet as filtrate while larger particles aggregate at highest gradient locations above the array. (d) Complications that could arise even at optimal sorting distance if magnetic properties of nanoparticles were not size-dependent.

Resolving these issues might require multiple passes of the sample through the array at different distances or obtaining samples that are uniform for at least one of

the parameters of size or magnetization. Finding the best distance for performing a separation of each pre-sort solution also requires magnetic and structural characterization of the pre-sort beforehand and careful optimization calculations based on the characterization results. The following chapters discuss these magnetic and structural characterization procedures and the optimizations that need to be done in preparation for separation experiments.

Chapter 4

Experimental Procedures

This chapter outlines the experimental procedures used for nanoparticle preparation, structural and magnetic characterization, and separation via the constructed Halbach array.

4.1 Nanoparticle synthesis and procurement

In most biomedical applications of magnetic fluids, the magnetic materials used are generally different types of iron oxides or ferrites because they demonstrate minimal toxicity inside the body. By far the most commonly used ferrites are magnetite (Fe_3O_4) and maghemite (γ-Fe_2O_3). Because magnetite can be oxidized to maghemite with only a small reduction in magnetic moment, the actual structure of particles in magnetic fluids usually involves the presence of both ferrites in an undefined ratio. For most applications, it is absolutely essential that magnetic particles be stable in suspension with regard to temperature changes and in the presence of uniform or non-uniform magnetic fields. In order to avoid settling or coagulation of particles, two different approaches are commonly used. The particle surface can either be coated with long organic chain molecule surfactants to produce a steric hindrance between particles or the particle surface can be charged to produce an electrostatic repulsion. In our study, we used both kinds of particles stabilized with such surface modifications.

The nanoparticle samples for the purposes of our study were obtained from two primary sources: Sigma-Aldrich company and a research group at Case Western Reserve University (CWRU). Preliminary testing of array performance and characterization sensitivity was performed using commercial iron oxide nanoparticles purchased from Sigma-Aldrich (product number 700320 and 700304). These relatively monodisperse particles were synthesized using a size-controlled method in accordance with Sun et al. [47], which involved a high-temperature solution phase reaction of iron (III) acetylacetonate in phenyl ether in the presence of hexadecanediol, oleic acid, and oleylamine. Small 7 nm Fe_3O_4 nanoparticles obtained midway in the reaction were used as seeds to grow larger nanoparticles in the precursors solution, giving rise to the 19 nm Fe_3O_4 nanoparticles reported by Gu et al [48]. From TEM, Sigma-Aldrich reported our manufactured nanoparticles to be of nominal sizes of 5 ($\pm$1) and 20 ($\pm$2) nm diameters, with a 1.5 nm thick coating of oleic acid as surfactant to avoid agglomeration. The particles were suspended in toluene with an initial concentration of 5 mg/mL, but could be diluted for separations by simply adding desired amounts of pure toluene without facing any settling problems.

Additional nanoparticle samples were obtained from Professor Anna Samia and her students at CWRU. While both toluene-based and water-based particles were obtained, we only dealt with Samia's water-based particles as they were closer to the sample types used in biomedical applications. Samia et al.'s paper [49] describes the synthesis of both these kinds of particles in detail. The toluene-based particles were synthesized using iron oleate, oleic acid, hexane and octadecene at a high temperature before cooling, washing with ethanol and centrifugation. Different sizes of nanoparticles were prepared by varying the relative amounts of oleic acid and iron precursor. The water-based particles were modified from the toluene-based suspension using aqueous basic reagents like ammonium hydroxide along with butanol, ethylamine and succinic anhydride. After these modifications, the particles were held suspended in water by repulsive electrostatic interactions over the pH range of 5 to 12, with an initial concentration of 5 mg/mL. A Beckman pH meter indicated a pH of 10.9 for our obtained water-based particles. Dilutions of these water-based samples for separations required careful monitoring of pH since pH disturbances disrupted electrostatic interactions causing large numbers of particles to quickly crash out of suspension. This settling was avoided by adding pre-made pH matched (pH 10.9) aqueous solution of sodium hydroxide (NaOH) in desired amounts.

These particles were selected for their ideal uniform spherical shape for which

small angle scattering curves can be readily modeled. In addition, working with Samia's water-based particles allowed us to test our improved channel made of Plexiglas and compatible only with water-based particles.

4.2 Structural Characterization

Structural characterization of magnetic nanoparticles to infer the particle size, shape and dispersion, is generally performed by analyzing transmission electron microscopy (TEM) images. Complementing a detailed TEM analysis, the structural properties of these particles can also be investigated, on both powder samples and liquid samples, using small angle x-ray scattering (SAXS) with an x-ray diffractometer (XRD) [50]. In fact, TEM image analysis only uses a small portion of the nanoparticle sample while small angle x-ray scattering allows characterization of the entire sample. This makes SAXS a more useful method for characterizing the total behavior of a sample of nanoparticles and we made extensive use of this technique as opposed to TEM image analysis. Here we review the methods followed and later we present data from both analyses in the results chapter.

4.2.1 Transmission Electron Microscopy and image analysis

Transmission Electron Microscopy is an imaging technique in which a beam of electrons is transmitted through an ultra-thin electron-dense specimen, interacting with the specimen as it passes through. TEM provides significantly higher resolution than optical microscopy and can be used to photograph nanostructures. TEM imaging was performed in Carnegie Mellon University by our collaborators on the commercial Sigma-Aldrich particles. Multiple images of the two samples were taken to cover a greater sample population. These images were then analyzed using ImageJ [51], an open-source image processing and analysis software developed by the National Institute of Health (NIH). ImageJ allowed us to remove the background and increase contrast so particles could be clearly distinguished and approximated as ellipses to calculate diameters of the suspended particles, as shown in Figure 4.1.

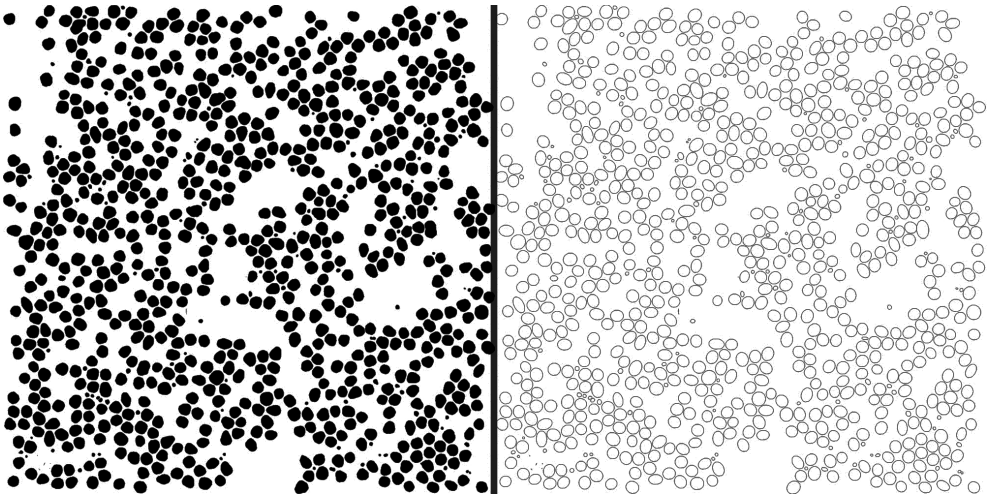

Figure 4.1: Two stages of Transmissions Electron Microscopy(TEM) image analysis performed using ImageJ analysis software. The picture to the right shows the particles in the left approximated as ellipses to extract diameter and distribution parameters.

Once the diameter values were obtained, a normalized histogram of particle diameters was created and fit to a lognormal distribution, given by

$$y = y_0 + A \exp\left[-\left\{\frac{ln(x/x_0)}{width}\right\}^2\right] \tag{4.1}$$

where y_0 is related to the offset due to background, A gives the peak probability of the peak of the normalized histogram, x_0 is the average particle diameter, and width $= \sqrt{2}$(dispersion) gives us information about the size dispersion of the particles. Our collaborators at Case Western performed similar analyses on their own particles and provided us with their results.

4.2.2 Small angle x-ray scattering

Structural characterizations were performed using a Rigaku Ultima IV 285mm X-ray diffractometer (acquired through NSF grant DMR-0922588 at Oberlin College) in the small angle X-ray scattering (SAXS) configuration. This compact XRD machine consists of a copper Kα x-ray vacuum tube coupled with a high-voltage power source to produce an x-ray beam of known wavelength and a sensitive detector to register scattered x-rays. The Ultima IV model also possesses interchangeable slit boxes with incident and receiving height limiting slits to eliminate non-correlated

scattered x-rays and direct the beam towards the sample stage to produce highly collimated x-rays. This XRD machine has numerous advantages including automated self-alignment and multiple attachment capabilities. The sample stage is held stationary while the x-ray tube and detector are moved in synchronicity to allow for easier measurement of powder and liquid samples.

For performing a small angle X-ray scattering experiment using the Ultima IV XRD, special SAXS geometry attachments are required. The SAXS geometry kit consists of SAXS sample holder, SAXS sample stage, vacuum path, and SAXS liquid and powder sample holders in addition to the standard X-ray setup. A diagram of this SAXS configuration put together in place into the XRD unit is seen in Figure 4.2. The vacuum path is an aluminum box kept under vacuum with x-ray transparent windows that reduces the amount of scattering from air separating the sample and detector. Unlike the standard sample stage using a reflection geometry, the SAXS stage utilizes transmission of the x-ray beam through the sample material to the detector, with detected beam intensity depending on size of the sample.

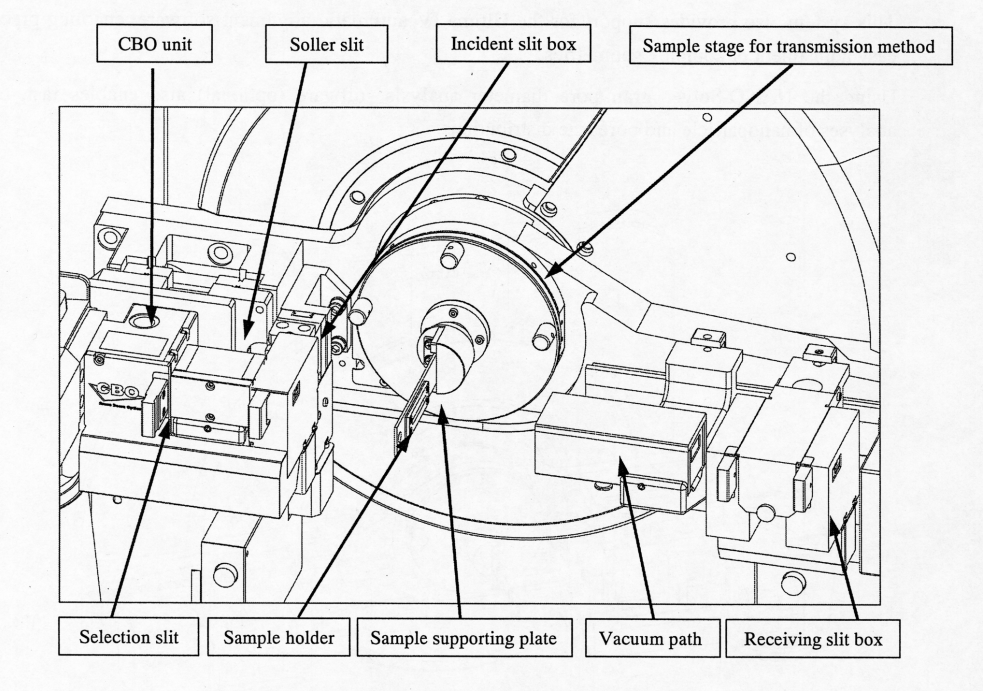

Figure 4.2: Configuration of SAXS geometry attachments in the XRD.

The viability of SAXS in the liquid phase using stainless steel liquid sample holders was tested by Rob Bond [52]. His results proved that successful SAXS patterns could be obtained under 300 minutes using a stainless steel design holder with screws and kapton windows for holding toluene-based particles.

However, for the water-based particles, we used a standard SAXS powder sample holder after drying the suspension to powder form on a mylar cutout in a crucible. The x-rays caused these water-based particles to crash out of solution during SAXS scans by interfering with the charge distributions that held the particles suspended. Therefore, scans of only their powder forms could be performed. All SAXS measurements were taken from 0.1 to 4 degrees 2θ with a step size of 0.02 degrees and a count rate of 1 minute per point, making each scan last about 200 minutes. The fits to measured curves were obtained using two different software: NANO-Solver and NIST SANS macros.

4.2.3 Curve fitting using NANO-Solver and NIST SANS macros

The Rigaku Ultima IV has an optional proprietary software package to interpret scattering data. The software, NANO-Solver version 3.7 [53], fits SAXS results to a model of spherical particles in a medium with a gamma (Γ) distribution of particle sizes. After the fit, it returns values for particle size, size distribution, packing fraction, nearest neighbor distance, and other quantities of interest. NANO-Solver also has the ability to account for two-phase systems by allowing the input of scattering length densities for both particle and solution. The Γ distribution function used in this software for analysis is expressed by Equation 2.27, the same equation used in the derivation of the final expression for scattering intensity.

If D is the independent size variable, D_0 is the average diameter when the scattering particles are spherical and M is the parameter of size distribution, then $M_{norm}[\%]$ gives the particle size dispersion when normalized by average size:

$$M_{norm}[\%] = \frac{\sqrt{\langle \delta D^2 \rangle}}{D_0} \times 100 = \frac{1}{\sqrt{M}} \times 100 \tag{4.2}$$

Despite the user-friendly platform of the proprietary software, NANO-Solver's fitting algorithms are not published, prohibiting a mathematical evaluation of the accuracy of its fit results. In addition, the program is not robust enough to deal with powder scan results. To test the accuracy of NANO-Solver predictions and to provide a framework to fit results from our powder scans, we used an open-sourced package from the National Institute of Science and Technology (NIST) that comes with the

Igor Pro data analysis software called NIST SANS macros [54], used predominantly for analysis of small angle neutron scattering (SANS) data, but which have been adapted for SAXS data.

The particle size distribution results from curve fits to NANO-Solver's gamma distribution and to NIST SANS macro's log-normal sphere model were reported by Kathryn Hasz [55] to agree within error for multiple SAXS datasets. These datasets included measured SAXS data of Sigma-Aldrich stock suspensions with a single mean particle size and of mixed suspensions with particles of multiple mean sizes. One important difference is that unlike NANO-Solver, NIST SANS macros allowed using the same framework that was verified to work for liquid samples, to then analyze SAXS data on powders of Anna-Samia's particles. The credibility of SAXS analysis using NIST SANS macros was further confirmed by good agreement with results from TEM on Anna-Samia's particles, shown later in the results section.

4.3 Magnetic Characterization using a VSM

The magnetic characterization of a magnetic fluid by plotting its magnetization curve can give us a rough idea about the magnetization of individual average nanoparticles in a sample and can allow distinguishing between solutions with different metals oxides. Magnetic characterization of samples was performed using a Lakeshore 7307 Vibrating Sample Magnetometer (VSM) shown in Figure 4.3, acquired using the NSF grant DMR-1104489 at Oberlin College. A VSM is based on the concept of Faraday's law of induction, which states that a time-varying magnetic flux induces a voltage signal in a detection coil nearby. In our magnetometer, magnetic fields of upto 1 Tesla applied to the vibrating sample were created using a large electromagnet. High voltage systems, fitted with cooling water, were in place to generate the large field. Although various temperature control settings were available, we performed all our measurements at room temperature.

The device's position and alignment were calibrated using a ferromagnetic Nickel standard of known magnetization in a field high enough to saturate the moment. Before measurement of any sample, careful adjustments were made to the already calibrated device to center the sample holder. Magnetic nanoparticle suspensions, placed in a holder and connected to a sample rod, were then vibrated back and forth in a region surrounded by several detection or pickup coils. This vibrating

magnetic sample resulted in time-varying magnetic flux, inducing an electric voltage signal through the pickup coils proportional to the sample's magnetic moment. This voltage signal was processed through a lock-in amplifier and other electronics built into the VSM. The Lakeshore 7307 VSM with accompanying IdeasVSM software were designed with a high level of automation, so the voltage signals were interpreted and the M vs. H curve of each sample directly plotted by the software, with remarkable reproducibility. The data points generated allowed us to easily calculate the sample's magnetization using the Langevin function given by Equation 2.7.

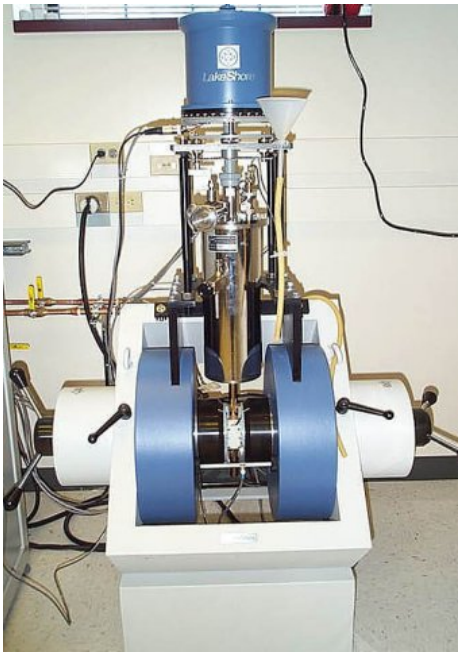

Figure 4.3: Lakeshore 7307 Vibrating Sample Magnetometer at Oberlin College.

For all our samples, we started out with a 50 μL volume of suspension and placed it in a Kel-F plastic holder made to hold liquid samples. Magnetic moment responses of $\sim 10^{-3}$ emu were reported for each sample, well above the 5×10^{-5} emu noise threshold of our magnetometer.

4.4 Nanoparticle separation procedures

In preparation for magnetic separation of nanoparticle suspensions using the Halbach array-channel assembly, magnetic nanoparticle stock solutions were structurally characterized using TEM and SAXS and magnetically characterized using magnetometry. Using results from the magnetic and structural characterization for any set of particle mixtures, calculations were done to figure out optimal field values

such that dipole-dipole interaction energy for larger particles at that field value exceeded k_BT by a few times, while U_{dd} for smaller particles was still less than k_BT. Once the optimum field value was calculated, an appropriate number of spacers were used underneath the channel to reach the necessary field. Finite element model calculations helped here by providing information about the ideal separation distance, along with the gradient value at the relevant field which allowed us to calculate the flow rate using Equation 3.4. A separation setup was then established with relevant flow channels at the right distances based on the samples to be used.

Once the separation setup was established, a mixture of two different stock suspensions was created and characterized using SAXS to get information about the pre-sort. It was then diluted, inserted into a syringe and pumped through the channel inlet at accurate flow rates using a syringe pump (Harvard Apparatus Syringe pump 11 Elite). The filtrate was collected from the outlet in a small vial and the residue was withdrawn from the channel at a high flow rate. Both the post-sort filtrate and residue were then characterized using SAXS to obtain volume fraction information to see how successful the single pass separation went.

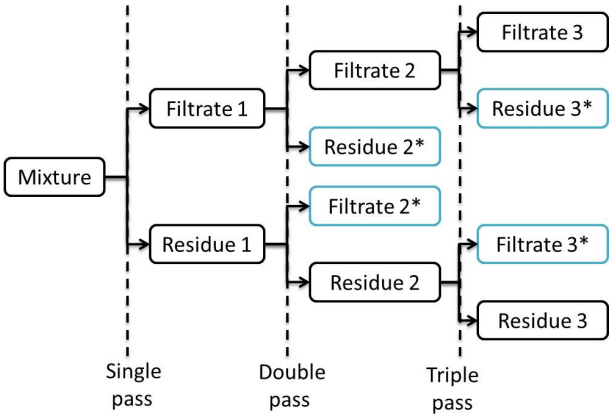

Figure 4.4: A schematic of multiple passes showing desired filtrates and residues produced in each step, along with the starred discarded products.

For multiple passes, the filtrates and residues from the single pass were passed through the array again separately, each giving rise to their own filtrates and residues, as shown in Figure 4.4. We would expect Filtrate 2 obtained from double pass to be more enriched in smaller particles than Filtrate 1. Few large particles with magnetization comparable to smaller particles might have entered into Filtrate 1 after a single pass but would hopefully be caught in the double pass as Residue 2*. Similarly, Filtrate 2* would most likely contain smaller particles with higher than usual magnetizations. The starred filtrates and residues would then mostly be a

collection of the few undesirable particles responsible for increasing magnetic and size variations of the mixture, and they can thus be discarded. When analyzing separation efficiency of the double pass, we have compared between Filtrate 2 and Residue 2 results as being the yields of that pass. Similarly, we have compared between Filtrate 3 and Residue 3 as yields of the triple pass.

Chapter 5

Results and Analysis

The results from structural and magnetic characterizations of magnetic nanoparticle suspensions and results of separation experiments have been presented, interpreted and discussed here. Later, a quantitative way to assess device performance based on use of various particle mixtures and number of passes has been explored through receiver operating characteristic curves.

5.1 Structural characterization results of nanoparticle suspensions

Structural characterization has been conducted using Transmission Electron Microscopy (TEM) and Small Angle X-ray Scattering (SAXS) techniques on Sigma-Aldrich's and Anna Samia's nanoparticle suspensions. SAXS curves of distinct particle stock suspensions have been experimentally found to be distinct and their behavior as expected for each suspension. NANO-Solver and our NIST SANS model's capapabilities have allowed us to pinpoint to a certain level of accuracy the types and volume fractions of different particles the suspensions contained, matching up quite well with information known about the stock suspensions used to create those mixtures.

5.1.1 TEM results of Sigma-Aldrich's and Anna-Samia's nanoparticles

Transmission Electron Microscopy image analysis has been performed on the imaging results received from Carnegie Mellon for two of our batch I samples - A7 and A20 (Sigma Aldrich's nominal 5 ± 1 nm and 20 ± 2 nm diameter particles). ImageJ software's image processing capabilities have allowed us to remove the grainy background of the carrier fluid and surfactant (toluene and oleic acid in our case), and increase contrast of the particles. Pixelated grains below a certain threshold size of 3 nm have been discarded for our analysis since they were most probably products of background noise. Representative images of the A7 and A20 samples after they have been processed are given below in Figure 5.1.

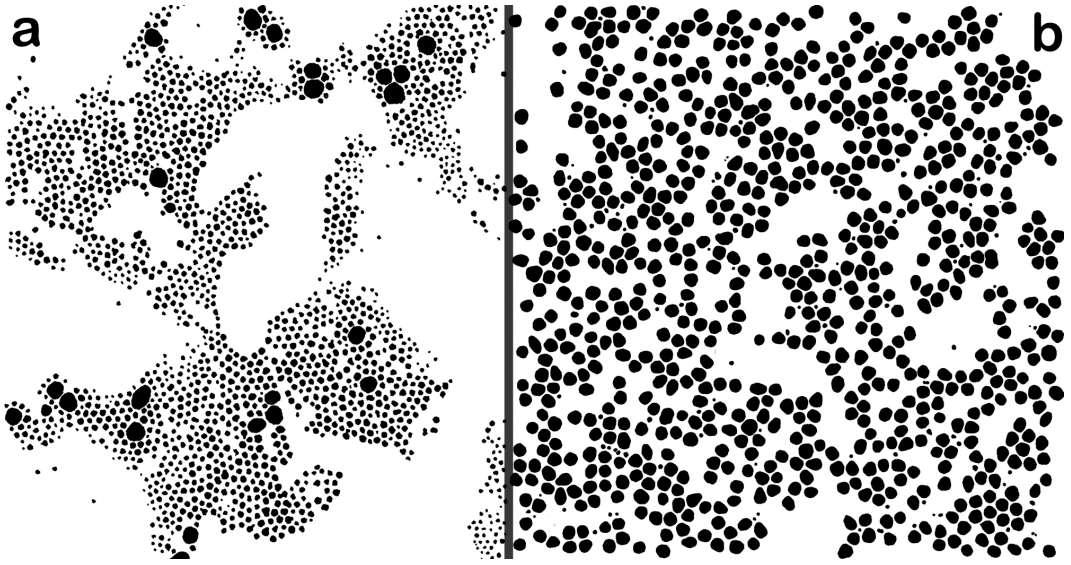

Figure 5.1: TEM images of Sigma Aldrich's A7 (shown in a) and A20 (shown in b) nanoparticles after ImageJ processing.

The smaller particle stock suspension (image a) seems to have contamination of a few big particles in it, and the larger particle stock seems to have a contamination of smaller particles in it. Although this points to the possibility of contamination of samples in the sample holder when performing the imaging experiments, it probably stems from the synthesis process of these nanoparticles. Gu et al. [48] describes the synthesis of monodisperse Fe_3O_4 nanoparticles in which 7 nm nanoparticles are used as seeds to grow larger nanoparticles in the precursor solution. The contamination of small particles in the large particle stock (image b) then makes sense in terms of looking at these particles as leftover seeds from the synthesis that did not grow

larger. Similarly, some of the larger particles in the small stock solution (image a) could be particles that went further into the reaction than intended.

Four TEM images (similar to image a in Figure 5.1) of the Sigma-Aldrich A7 particles have been analyzed, and the data obtained from all four images have been used in creating a single normalized histogram of particle diameters given in Figure 5.2. The lognormal fits to the TEM images suggest an average diameter for the smaller particle sample to be closer to 7 nm rather than the nominal 5 nm reported by Sigma-Aldrich. This result strongly matches with the results we obtain from small angle x-ray scattering (SAXS) on the small particle mixture (see table 5.2).

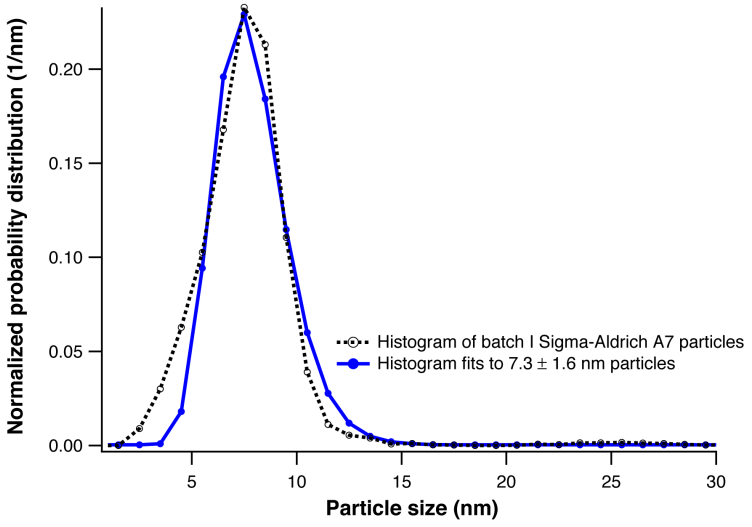

Figure 5.2: Lognormal fit to the histogram data combined from four images of nominal 5 ± 1 nm particles (A7) purchased from Sigma-Aldrich. The fit indicates an average particle size of 7.3 ± 1.6 nm, comparable to the result 7.4 ± 1.3 nm obtained from SAXS. The number of larger particles is comparatively so low that their probability distribution is really small.

Similarly, three TEM images of Sigma-Aldrich A20 particles (similar to image b in Figure 5.1) have been analyzed, and the data from the three images have been used in creating a single normalized histogram of particle diameters given in Figure 5.3.

However, our lognormal fits to histograms of particle size from the Aldrich A20 stock in Figure 5.3 suggest a much larger size of ∼25 nm, that does not match with the 20 nm diameter reported by Aldrich, or with NANO-Solver fits to SAXS experimental data collected on the same sample (which also point to a 20 nm average particle diameter). This large discrepancy was found to be a result of ImageJ analysis taking most of the larger ill-formed particles and approximating ellipses out of their

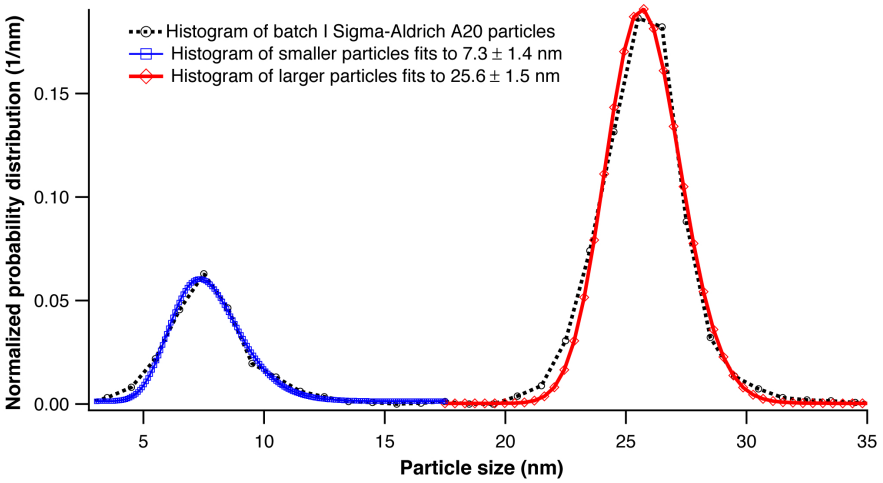

Figure 5.3: Lognormal fit to the histogram data combined from three images of nominal (20 ± 2) nm particles (A20) purchased from Sigma-Aldrich indicates an average particle size of 25.6 nm, with a contamination of smaller 7.3 nm particles.

major diameter, making our entire analysis to be skewed towards a larger diameter size. In addition, TEM is an imaging technique that relies on selectively sampling a few hundred particles that do not overlap during imaging to make a quantitative statement about billions and billions of particles. Therefore, TEM results generally have a sampling bias and are useful for determining particle shapes and at best, providing a rough estimate of particle size.

Despite this discrepancy, the dispersions for both samples obtained from TEM analysis seem to point towards results similar to those obtained from SAXS fits. For the A20 stock suspension, isolating bigger particles from the TEM image and fitting them to a lognormal separately results in a smaller dispersion (∼6%) than that given by SAXS (∼9%), which makes sense because SAXS scans the entire suspension of 20 nm particles with few 7 nm seeds interspersed in them, averaging to a larger dispersion. The results from the two structural characterization techniques typically complement each other and help make greater sense of the data.

Results from TEM image analysis of Anna Samia's particles performed by our collaborators have also been reported during sample procurement (Table 5.1), and they agree well with SAXS results that we have performed (see Table 5.2).

Samples	Designated Name	Measured average particle size
Anna Samia	S15	14.9 ± 0.9 nm
	S26	24.0 ± 1.5 nm

Table 5.1: TEM characterization of Anna-Samia's nanoparticles.

5.1.2 SAXS results of stock suspensions and mixtures

After TEM analysis on each of our stock suspensions, the validity of TEM results has been confirmed by using our primary analysis technique of small angle x-ray scattering. Figure 5.4 shows SAXS measurement results on four Sigma-Aldrich stocks solutions suspended in toluene and measured in our liquid sample holder. Similarly, Figure 5.5 shows SAXS measurements on two of Anna Samia's particles dried to a powder form and measured in the powder sample holder.

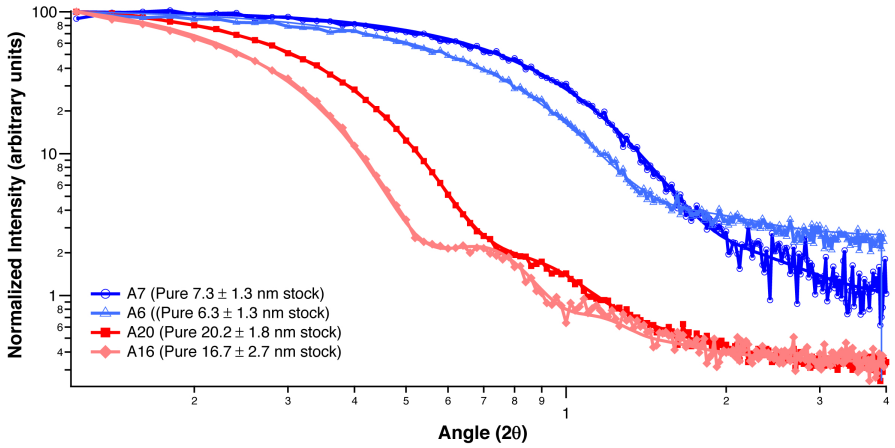

Figure 5.4: Small angle x-ray scattering results of four Sigma-Aldrich stock suspensions used in our separations show variations in SAXS patterns, relating to their particle size and dispersion. The fits to measured curves have been obtained using NANO-Solver software.

Table 5.2 contains a list of information extracted from fits to SAXS results on stock suspensions of Sigma-Aldrich and dried powders of Anna Samia's nanoparticles. The SAXS data for Sigma-Aldrich's suspensions have been fitted using NANO-Solver's gamma distribution (see Equation 2.27) and Anna Samia's dried powders to NIST SANS macro's lognormal sphere model. The fits allow us to see variations between individual Aldrich batches even though they were the same product, just purchased at different times. A number of SAXS characterization tests have been performed on each of these samples over the course of many separations, yielding

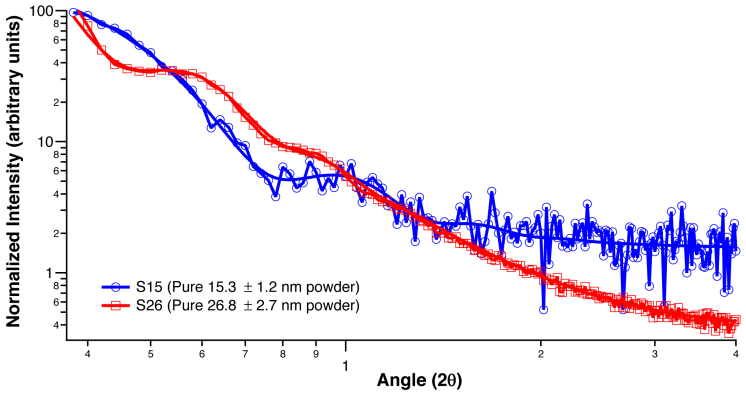

Figure 5.5: Small angle x-ray scattering results of two Anna Samia's two stock suspensions dried to powder form. Fits to SAXS pattern were obtained using NIST SANS Macros.

greatly reproducible fits and assuring us that SAXS is a reliable characterization method for these liquid and powder samples.

Batch	**Designated Name**	**Nominal size**	**Measured average particle size**	**Fits**
Aldrich I suspension	A7	5 nm	7.4 ± 1.3 nm	NANO-Solver
	A20	20 nm	20.2 ± 1.8 nm	
Aldrich II suspension	A6	5 nm	6.3 ± 1.3 nm	NANO-Solver
	A16	20 nm	16.7 ± 2.7 nm	
Anna Samia powder	S15	15 nm	15.3 ± 1.2 nm	NIST SANS macros
	S26	24 nm	26.8 ± 2.7 nm	

Table 5.2: SAXS characterization of Sigma-Aldrich's and Anna Samia's stock samples show how particle mixtures vary from nominal values, and also show their size dispersion in samples.

Using the two batches of Aldrich's nominal 5nm and 20nm diameter particles suspended in toluene, mixtures of small and large particles have been created in different proportions to compare their SAXS curves. As we can see in Figure 5.6, we can visually examine whether a mixture contains a majority of smaller particles or larger particles just based on comparing the undulation patters of the mixture's SAXS curves with the patterns of the pure stocks. This figure contains mixtures E, F and G prepared from A7, A6, A16 and A20 stocks in various volumetric proportions characterized in more detail in Table 5.3. It is important to note that background noise was measured for pure toluene in the same liquid sample holder in which these nanoparticle samples were measured. This background was subtracted from all runs before performing a particle size analysis in NANO-Solver.

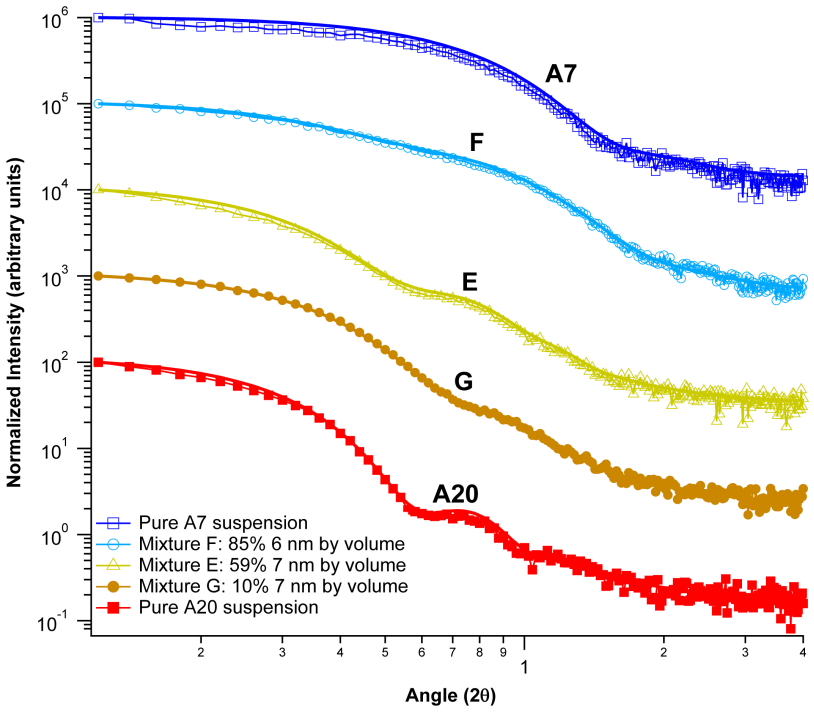

Figure 5.6: Small angle x-ray scattering results of mixtures containing different proportions of Sigma Aldrich's 7nm and 20nm particles. The fit parameters have been obtained using NANO-Solver software.

Letter Designation	**Stock suspensions mixed**	**Measured average particle size**	**Volume fraction**
E	A7 and A20	7.6 ± 1.7 nm 20.3 ± 1.7 nm	59% 41%
F	A6 and A20	6.3 ± 1.3 nm 18.3 ± 2.7 nm	85% 15%
G	A7 and A16	7.2 ± 1.0 nm 16.6 ± 2.9 nm	10% 90%

Table 5.3: Characterization of mixtures made from Sigma-Aldrich stock suspensions.

5.2 Magnetic characterization results of nanoparticle suspensions

The net moment of particle stock suspensions as a function of applied magnetic field has been measured using a Lakeshore 7307 VSM, with the suspensions showing superparamagnetic-like behavior. 50 μL volume of each of the 5 mg/mL concentrated suspensions were used for measurement. Figure 5.7 illustrates the plots of mass magnetization (measured in emu/g) vs. applied field (measured in Oersteds) along with their Langevin fits (Eqn 2.7) for each of the four stock suspensions we purchased from Sigma-Aldrich to be used in our separation experiments. In addition, the results from Langevin fitting to those curves have been summarized in Table 5.4 to give the mass magnetization of the solution and moment per average individual particle.

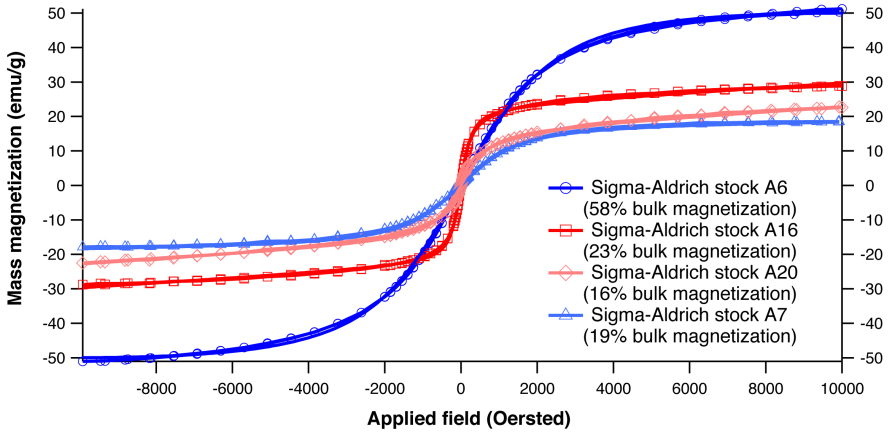

Figure 5.7: Magnetometry of Sigma-Aldrich's stock suspensions gives mass magnetizations that can be compared to that of pure bulk magnetite (91 emu/g) to assess the "magnetic quality" of the samples.

Batch	Sample Label	Nominal size	Mass magnetization (emu/g)	Moment per particle (Bohr magnetons)
I	A7	5 nm	18.8 ± .2	7.4×10^3
	A20	20 nm	16.4 ± 0.2	1.5×10^4
II	A6	5 nm	58 ± .5	4.7×10^3
	A16	20 nm	23.2 ± .1	4.1×10^4

Table 5.4: Magnetic characterization results of Langevin fits to **M** vs. **H** curves, obtained by magnetometry on Sigma-Aldrich suspensions of 50μL volume. The different batch numbers correspond to separate purchases of these particles and the nominal size (diameters) refer to Sigma-Aldrich's description of the product.

Similarly, Figure 5.8 shows the plots of mass magnetization (measured in emu/g) vs. applied field (measured in Oersted) along with their Langevin fits for two of Anna Samia's water based stock nanoparticle suspensions we used in our separation experiments. The Langevin fits have been plotted as well, and the data from those fits are in Table 5.5.

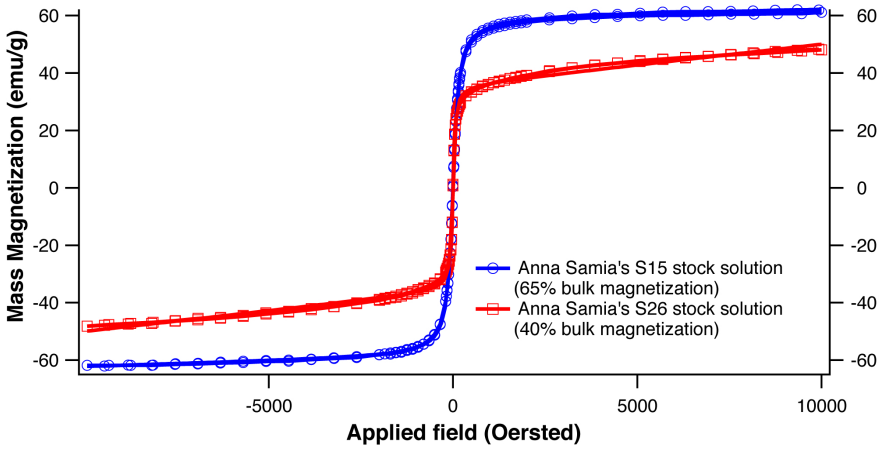

Figure 5.8: Magnetometry results of Anna Samia's stock suspensions allow similar comparison of mass magnetization of samples to that of bulk magnetite.

Stock suspensions	**Total magnetic moment (emu/g)**	**Moment per particle (Bohr magnetons)**
Anna Samia's 15.3 nm stock	59.2 ± 0.1	6.9×10^4
Anna Samia's 26.8 nm stock	36.0 ± 0.2	1.6×10^5

Table 5.5: Magnetic characterization results of Langevin fits to **M** vs. **H** curves, obtained by magnetometry on Anna Samia's stock suspensions.

These data about moment per particle and mass magnetization extracted from the Langevin fits to measured values, along with the particle size data from SAXS fits provide us with enough information to calculate relevant array-channel distances for each separation process that use these samples.

5.3 Separation results

To test the performance of the constructed array with previously characterized nanoparticle stock suspensions, we have conducted a series of separation experiments

and then used SAXS as a post-separation analysis method to quantify degree of separation. Single pass experiments have been performed by passing the mixed suspensions once through the channel at optimal distances above the array and then characterizing the post-sort filtrate and residue. Multiple pass experiments have also been performed to test the limits of the device by passing the post-sort filtrate and residues from the single pass through the array multiple times. The rate of passing solutions through the channel has been calculated using Equation 3.4 for each set of separations.

First we summarize our results from separations of toluene-based suspensions from Aldrich that use our toluene-compatible glass channel. Later, we discuss results from separation of water-based suspensions from Anna Samia that use our water-compatible Plexiglas channel.

5.3.1 Toluene-based nanoparticle suspensions

Our first separation has been done using Sigma-Aldrich's batch I 7.4 nm and 20.2 nm (samples A7 and A20) toluene-based particles mixed in a 59% A7 and 41% A20 ratio by volume. Based on SAXS and magnetometry characterization results from Tables 5.2 and 5.4, the optimal field has been calculated to be ∼110 mT with channel distance at 0.15 cm steel plate away from the array. Flow rate has been calculated to be below .2 mL/min so a rate of 0.1 mL/min has been used. This takes around 20 minutes to sort a diluted 2 mL pre-sort mixture.

As shown in Figure 5.9, SAXS measurements of the unmixed suspensions clearly indicate differences in the form factor beating as expected for nanoparticles of different diameters (patterns 1 and 4). The mixture of the two (pattern 3) displays an intermediate pattern. Single pass of this mixture 3 has led to a significant change in small angle scattering of the analyte/filtrate (pattern 2). On doing a NANO-Solver fit to extract quantitative data, the 7 nm particles in the filtrate have showed substantial enrichment starting from a volume fraction of only 59% in the original mixture to 81% just after a single pass. These results have been quantified in Table 5.6 and are exciting in that just a 20 minute single pass processing of a 2 mL pre-sort mixture can cause a big difference in the sample composition. In addition, separation success could be seen roughly even from the color of the sample. The 7 nm pure stock solution (1) looks much lighter than the 20 nm stock solution (4). Their mixture is still

dark (3) but on separation, the filtrate (2) shows a much lighter coloration, closer to (1) and indicative of a large volume fraction of the smaller 7 nm particles in it.

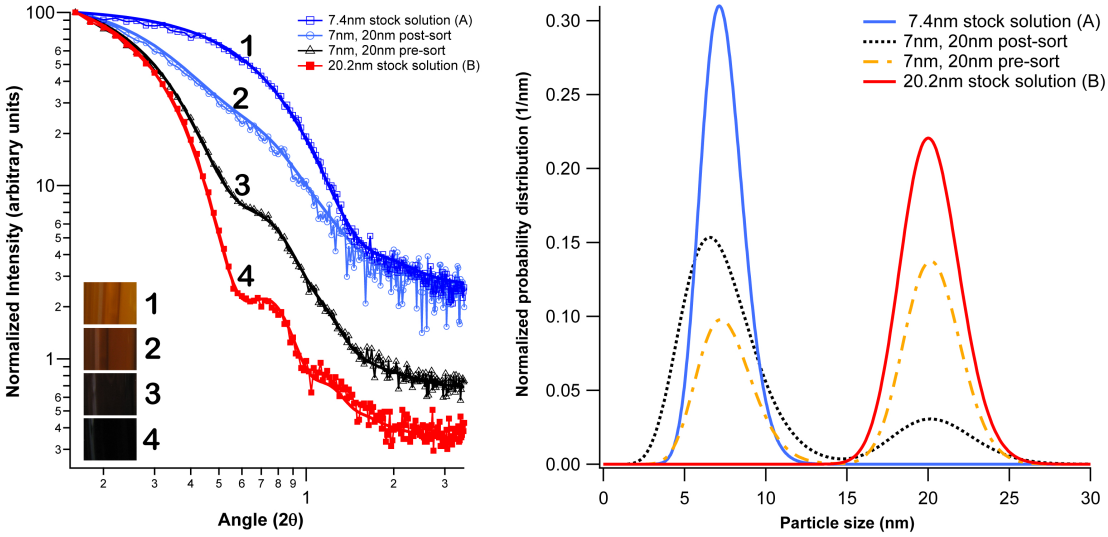

Figure 5.9: SAXS curves (left) and particle distributions (right) of Sigma Aldrich's A7 and A20 suspensions, mixtures and their post-sort filtrate. The fits have been obtained using NANO-Solver software.

Solution	**Measured average particle size**	**Volume fraction**
7.4 nm stock solution (A7)	7.4 ± 1.3 nm	
20.2 nm stock solution (A20)	20.2 ± 1.8 nm	
Pre-sort mixture (A7+A20)	7.6 ± 1.7 nm 20.3 ± 1.7 nm	59% 41%
Post-sort filtrate	7.2 ± 2.2 nm 20.4 ± 2.4 nm	81% 19%

Table 5.6: SAXS characterization results of a single pass separation of 59% : 41% mixture of Sigma-Aldrich stock suspensions A7 and A20.

One concerning piece of information in this characterization of post-sort filtrate is its rise in dispersion, making it much less uniform than the stock solution we started out with. This certainly makes the filtrate sample not very usable for a number of applications. This increase in dispersion is most probably due to the non-uniform 7 nm contaminants present in the A20 stock solution, which must have gone into the filtrate.

For the sake of testing reproducibility and comparing between different Aldrich batches, another particle pre-sort mix made up of 6.3 nm and 16.7 nm stock suspensions (Batch II, A6 and A16) in a 57 % : 43% ratio by volume has been put through a single pass using 1 steel plate 0.15 cm away from the array at a field of ∼110 mT. The residue has been obtained in suspended phase by simply withdrawing the suspension with chained particles that do not make it all the way to the flow-through. On characterizing and comparing results from the earlier separation of A7

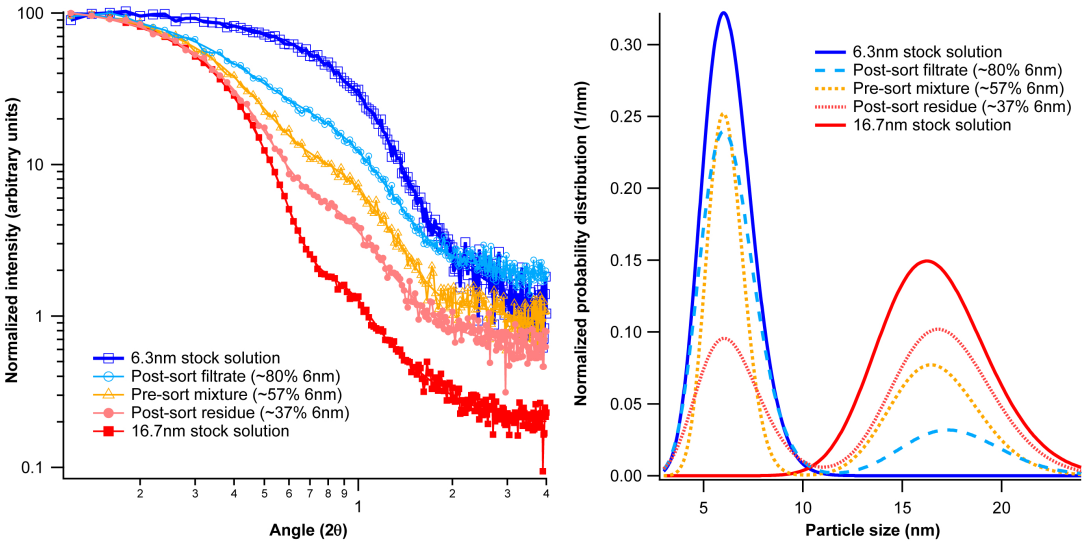

Figure 5.10: SAXS curves (left) and particle distributions (right) of Sigma Aldrich's A6 and A16 suspensions, mixtures and their post-sort filtrates and residues. The fits have been obtained using NANO-Solver software.

Solution	**Measured average particle size**	**Volume fraction**
6.3 nm stock solution (A6)	6.3 ± 1.3 nm	
16.7 nm stock solution (A16)	16.7 ± 2.7 nm	
Pre-sort mixture (A6+A16)	6.1 ± 0.9 nm 16.7 ± 2.2 nm	57% 43%
Post-sort filtrate	6.3 ± 1.4 nm 17.6 ± 2.5 nm	80% 20%
Post-sort residue	6.4 ± 1.6 nm 17.2 ± 2.5 nm	37% 63%

Table 5.7: Characterization of a single pass separation of 57% : 43% mixture of Sigma-Aldrich stock suspensions A6 and A16 shows reproducible results when compared to separation of a 59% : 41% mixture of A7 and A20.

and A20 (in Table 5.6) with the results from separation A6 and A16 (in Table 5.7),

we can see that both the pre-sort mixtures have started out with a relatively equal proportion of smaller and larger particle stocks by volume and have both resulted in a substantial enrichment of small particles in the post-sort filtrate, yielding a solution of ∼80% small particles by volume. This is an important result demonstrating the reproducibility and reliability of our separation technique and the level of control we have over each separation, distinguishing it from commonly used techniques of magnetic separation which can be highly random in their performance.

Seeing that single passes could only get us to around 80% small particles in the post-sort filtrate, pre-sort mixtures have been passed through the array multiple times to obtain post-sort filtrates, and then characterized to see if the fraction of small particles would increase beyond 80%. It has been found that multiple passes of Sigma-Aldrich do improve the volume fraction of small particles in the filtrate but cannot do so beyond the high limits of around 88%. However, an exciting result is that even pre-sorts with substantially low volume fraction of small particles can be enriched to reach the those high limits. The separation below describes such an enrichment.

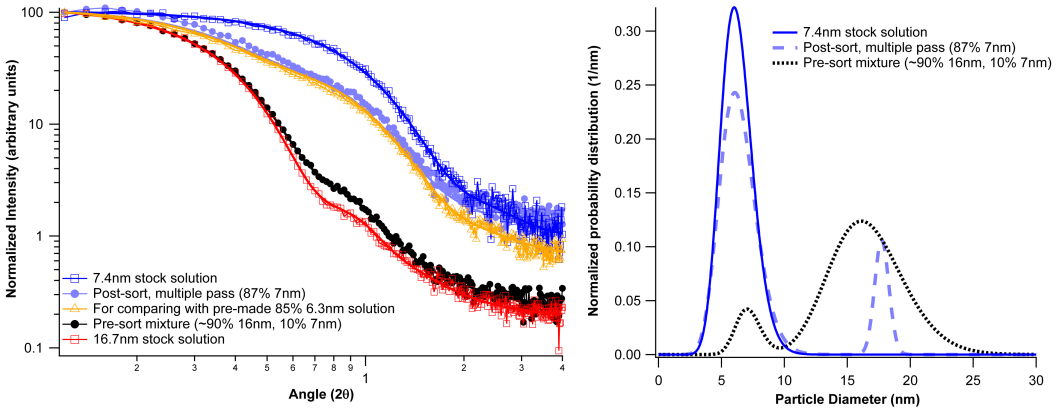

Figure 5.11: SAXS curves (left) and particle distributions (right) of Sigma Aldrich's A7 and A16 suspensions, mixture and the multiple pass post-sort filtrate. The fits have been obtained using NANO-Solver software.

Multiple pass separations of a highly skewed pre-sort mixture of 10% A6 and 90% A16 suspensions have been performed, again at ∼110 mT fields, where a massive enrichment of small particles in the filtrate has been seen leading to an 87% by volume of the A6 particles, as shown in Figure 5.11 and Table 5.8. The 20% dispersion of small particles seen in the stock solution was preserved in the filtrate, while the dispersion of larger particles was reduced to ∼3%, meaning that only a fraction of the larger particles with unusually low magnetization could not be filtered by this process.

Solution	**Measured average particle size**	**Volume fraction**
7.4 nm stock solution (A7)	7.4 ± 1.3 nm	
16.7 nm stock solution (A16)	16.7 ± 2.7 nm	
Pre-sort mixture (A7+A16)	7.2 ± 1.0 nm 16.6 ± 2.9 nm	10% 90%
Post-sort filtrate	7.4 ± 1.5 nm 19.2 ± 0.6 nm	87% 13%
Compare to pre-made 85% 6 nm mixture	6.3 ± 1.3 nm 18.3 ± 1.7 nm	85% 15%

Table 5.8: SAXS characterization results of a multiple pass separation of a highly skewed mixture of Sigma-Aldrich stock suspensions A7 and A16.

Having explored the sorting of a mixture of two distinct toluene-based stock suspensions, the array's capabilities in purifying a single stock suspension was examined. This could be done either by narrowing down the dispersion of a sample or introducing some cutoff size such that particles bigger than the cutoff are depleted in the filtrate, yielding a solution purer than commercially obtained particles. Being able to sharpen size dispersion would be extremely advantageous in most applications of nanoparticles and in nano-manufacturing. In addition, being able to maintain a cutoff would be helpful for making better contrast agents in magnetic particle imaging. However, discriminating between particles of very similar magnetization and size requires selective chaining of particles by making the dipole-dipole energies of only some large-particle interactions to be greater than thermal energy.

For the purposes of testing purification capacity, some preliminary multiple pass tests have been performed on a new Sigma-Aldrich batch of nanoparticles. The gamma distributions of multiple pass filtrate and single pass residue acquired from NANO-Solver's fits to SAXS curves have been shown in Figure 5.12. The results indicate a slight shift in the first pass residue towards a larger average particle size and a small reduction in dispersion of the multiple pass filtrate accompanied by a shift towards smaller average particle size. Using the toluene-compatible glass channel only allows separation at specific large sub-optimal distances above the array. Future work should take advantage of the newer water-compatible channel design that allows finer control of array-channel distance to try and purify the stock suspensions.

After various separations on toluene-based suspensions, we move on to results

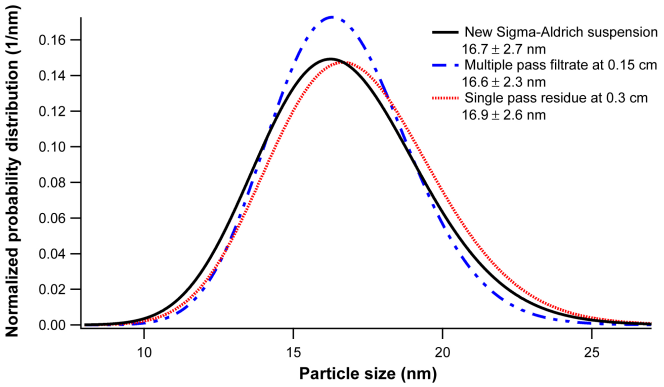

Figure 5.12: Particle distributions of stock, filtrate and residue from purification attempts on a new Sigma-Aldrich batch of particles.

obtained from separation experiments on Anna Samia's water-based nanoparticle suspensions.

5.3.2 Water-based nanoparticle suspensions

After acquiring water-based particles from Anna Samia and her students at CWRU, multiple pass separations have been tested with a new water-compatible Plexiglas channel at a higher field and gradient than allowed by the older glass channel. Anna Samia's nanoparticle suspensions, as opposed to Sigma-Aldrich's, have the advantage of tighter distributions of particle sizes without any size overlaps, along with very different magnetizations of the two suspensions. This type of particle behavior makes it much easier to sort the two fractions, even with a device that has less discriminating capacity.

Calculations from magnetometry results of the pure samples suggest using more than 2 plates under the channel for a total array-channel distance of greater than .30 cm at fields of ∼50 mT to prevent significant dipole-dipole interactions between small and large nanoparticles while still causing significant clumping of larger particles. A roughly 50:50 ratio mixture of 15.3 nm and 26.8 nm stocks has been created and diluted to make it amenable for separation. After SAXS characterization of the initial mixture, first and second passes have been done with 2 plates underneath the new channel. SAXS scans of first and second pass filtrates indicated enrichment of small particles from the initial 54% to 66% to 90%, while larger particles were enriched in the residue from an initial 46% to 75% in the first pass. To improve the quality of filtrate in the 3rd pass, the separation has been started out with a single plate below the channel to let the remaining big particles chain, and plates have been

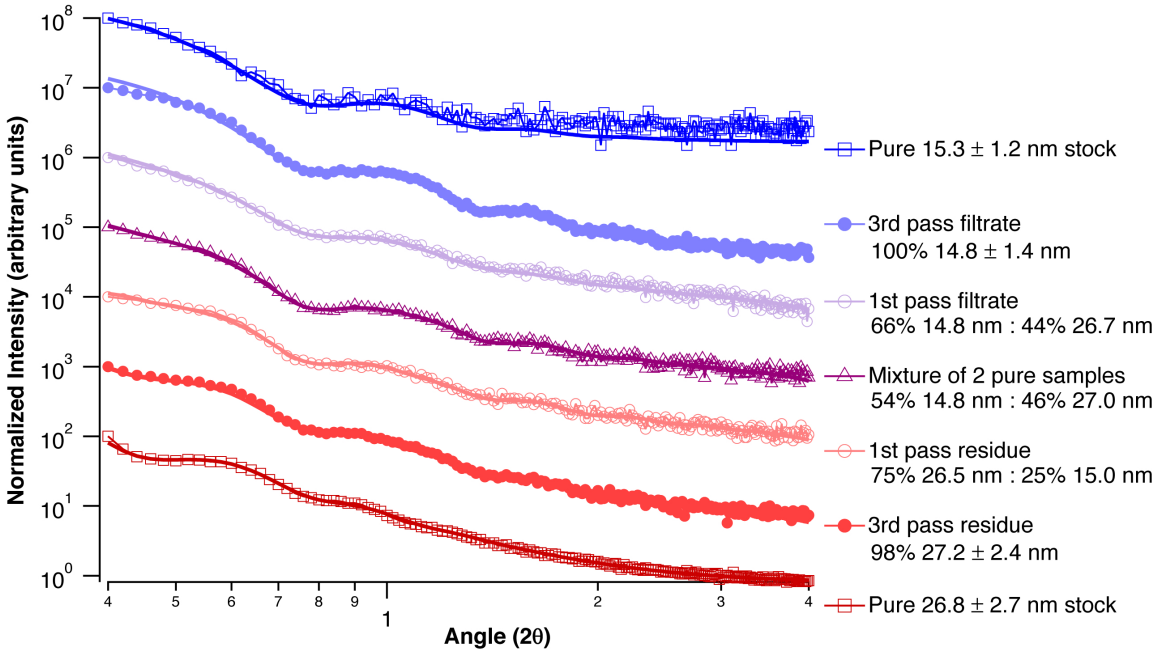

Figure 5.13: SAXS curves of Anna Samia's particles during different stages of the separation process. Solid curves are fits to NIST SANS macros.

Solutions	**Measured average particle size**	**Volume fraction**
15.3 nm stock solution (S15)	15.3 ± 1.2 nm	
3rd pass filtrate	14.8 ± 1.4 nm	100%
1st pass filtrate	14.8 ± 1.5 nm	66%
	26.7 ± 2.4 nm	44%
Mixture of two pure samples	14.8 ± 0.9 nm	54%
(S15+S26)	27.0 ± 1.6 nm	46%
1st pass residue	15.0 ± 0.8 nm	25%
	26.5 ± 2.1 nm	75%
3rd pass residue	15.1 ± 0.5 nm	2%
	27.2 ± 2.4 nm	98%
26.8 nm stock solution (S26)	26.8 ± 2.7 nm	

Table 5.9: Characterization of a triple pass separation of ~50:50 mixture of Anna Samia's 15 and 26 nm particle suspensions. These results come from SAXS measurements performed on dried powder forms of water-based suspensions in a powder sample holder. The fits to curves were obtained from NIST SANS Macros.

added one by one to slowly let out smaller particles that might have been trapped in the chain. A similar process for the residue has led to the final result of 100% 14.8 nm in the filtrate and 98% 27.2 nm in the residue, an almost perfect separation of particles.

After having obtained SAXS characterization results from a number of separation experiments using the Halbach array and after having discussed them separately, we would like to develop a quantitative way to assess the overall performance of our device taking into account not just the separation experiments highlighted above but all our recorded separation datasets with the device. The section below provides the methodology for such an analysis.

5.4 ROC Analysis

Receiver Operating characteristic (ROC) analysis is a statistical methodology that comes out of signal detection theory, and is commonly used in the analysis of medical imaging technology [56, 57] . It is used to evaluate the discriminatory performance of medical imaging tests to be able to sort images by presence or absence of tumors, essentially "signals" or "noise" [58]. We have adapted the ROC analysis procedures in the case of our Halbach device, using the volume fractions from SAXS characterizations of the filtrate and residue for each separation. Such an analysis will be able to examine the array's performance in different separation conditions through several possible sorting outcomes and find optimal procedures for future nanoparticle sorts.

When considering the results of a particular test or sort in two populations of small and large particles, we will rarely observe a perfect separation between the two groups with all small particles ending up in the filtrate and all large particles in the residue. If we assume that we're trying to separate small particles out of a mixture of small and large particles, then for every possible outcome of sorting we can identify four cases. There will be small particles in the filtrate (true positive), large particles in the filtrate (false positive), large particles in the residue (true negative) and small particles in the residue (false negative). The most commonly used figures-of-merit for sorting accuracy are "sensitivity" or the true positive fraction (TPF), and "specificity" of the sort [56]. In our case, sensitivity is the probability that small particles end up in the filtrate and specificity is the probability that large particles

end up in the residue, given by the equations below:

$$Sensitivity(TPF) = \frac{TP}{TP + FN} = \frac{Filtrate_{small}}{Filtrate_{small} + Residue_{small}} \tag{5.1}$$

$$Specificity = \frac{TN}{TN + FP} = \frac{Residue_{large}}{Residue_{large} + Filtrate_{large}} \tag{5.2}$$

$$FPF = 1 - Specificity \tag{5.3}$$

An ROC curve is a plot of the true positive fraction (TPF) in the y-axis with respect to the false positive fraction (FPF) in the x-axis. A diagonal line in this plot represents a completely random mix where no discrimination of particles is achieved. Similarly, a point on the top left of the plot represents the best possible discrimination of particle mixtures where all small particles end up in the filtrate and all large particles end up in the residue.

In Figure 5.14, datapoints for each of our separation experiments have been plotted according to the procedure described above, to assess our Halbach device performance on various particle mixtures using single and multiple passes at different array-channel locations. For single passes, each individual data point in the plot represents the characterization results of filtrate and residue obtained from a single separation performed with the array. For multiple passes, each datapoint represents characterization results of filtrate and residue obtained from two distinct separations, one done on the single pass filtrate and one on the single pass residue, as explained in Figure 4.4. Our separations can be categorized into four different cases, each containing datapoints with similar levels of separation success. Excluding the diagonal line, four different curves have been created in the figure, just as a guide to the eye for visually separating the four cases. There are a few general statements that could be made from the analysis of these curves, explained below.

Single passes of ∼50:50 mixtures of particles at sub-optimal heights yield poor separation results compared to single passes of similar mixtures performed at optimal height, which can be seen visually by comparing the lower two curves in the plot. The correct adjustment of height seems to be very important for maximizing the sort ratio of particles to reach a desired level of separation. There is ongoing work to optimize and obtain finer control of array-channel distance using a height-adjustable channel configuration for the water-based nanoparticle separations, as explained later in Chapter 6.

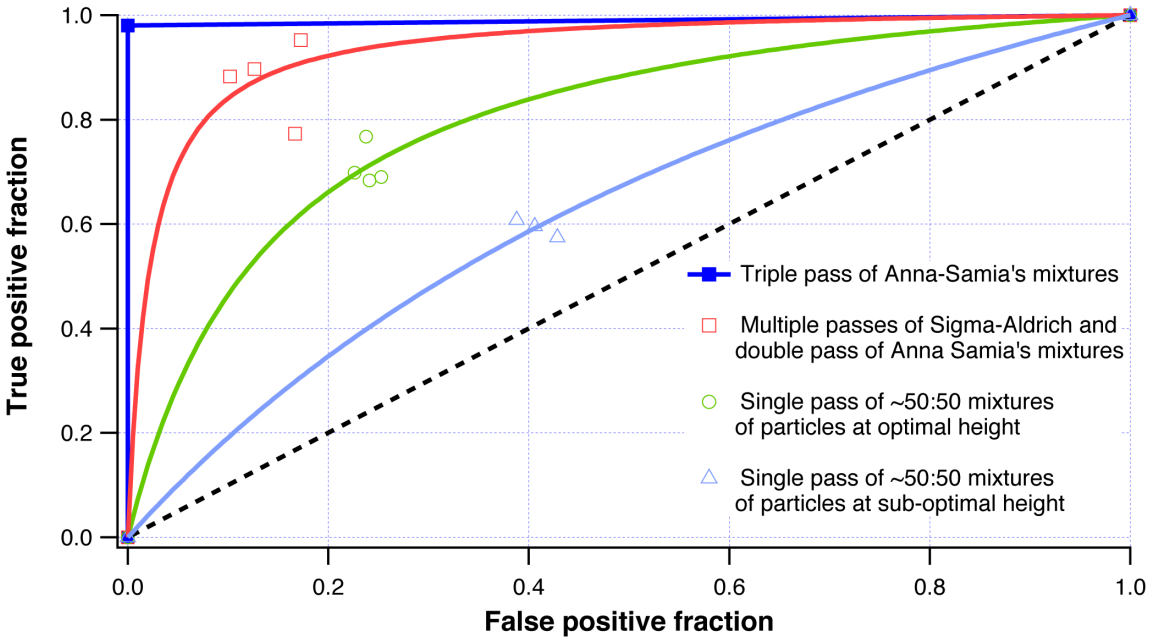

Figure 5.14: ROC curves for the Halbach array's separation performance with different particle mixtures at different array-channel distances.

We can also see in the Figure that multiple passes of mixtures significantly improve the array's separation performance, when compared to single passes of the same mixtures. This is seen visually as the jump from the green curve for single pass of Sigma-Aldrich suspensions to the red curve for multiple passes. Both curves represent separations done at the optimal distance from the array.

Using nanoparticle samples from two different sources has allowed us to compare the device's ease of separation or success based upon the quality of samples. With Sigma-Aldrich's 50:50 mixture, multiple passes (at least three) were required to reach the red curve while just a double pass of Anna Samia's particle mixture seemed to get us to the same level of sorting performance. Likewise, just a triple pass of Anna Samia's particles leads to an almost perfect separation with 100% small particles in the filtrate and 98% large particles in the residue according to our SAXS results, shown by the top blue curve. It does make sense that a device with the capacity to discriminate between nanoparticles based upon their size and magnetic properties does better when particles are clearly very distinct in these characteristics.

Thus, we can see that ROC curves can offer a quantitative description of our device's separation performance in different circumstances by examining several possible outcomes. Furthermore, an ROC analysis can offer us strategies to pursue for future separations of nanoparticles to maximize sort ratio and efficiency.

Chapter 6

Conclusions and Future Work

6.1 Conclusions

Magnetic nanoparticles smaller than 30 nm are particularly important for biomedical applications. This thesis has demonstrated the utility of our novel method for separating suspensions of small magnetic nanoparticles in that size regime, based on their size and magnetic moments. Our design and construction of an inverted linear Halbach array has showed that its low flux side contained a low magnetic field with a high field gradient in conjunction, two things that are critical for our method of magnetic separation to work. The magnetic characteristics of the assembly have also agreed well with finite element method calculations and thus allowed for accurate modeling of magnetic forces.

We have also outlined some of the important results obtained using our device in the separation of Sigma-Aldrich's toluene-based particles and Anna Samia's water-based particles. We have found out that multiple passes of particle suspensions, when compared to single passes through the device, improved sorting ratios of particles. However, multiple passes of particle suspensions could only discrimate them upto a certain level if suspensions had possible non-correlated variations in size and magnetic moments. In these sorts, we have realized that being at sub-optimal field and gradient values adversely affected sorting efficiency and that sort ratio could be improved significantly by being at the calculated optimal array-channel distance. In addition, we have discovered that mixtures containing two particle distributions around average sizes separated by 10 nm, having clear differences in their magnetic moments, could be sorted almost perfectly by our device in just three passes.

Most separation techniques try their best to avoid inter-particle interactions as a complicating factor during separations. However, we have made conscious use of field-induced dipole-dipole interactions between our larger superparamagetic particles to reversibly aggregate and separate them. Creating particle chains helped us maximize forces on them to bring them down to the channel bottom quickly, increasing our throughput by orders of magnitude compared to techniques that use magnetic forces on single particles.

Finally, we were also able to quantitatively access the performance of our device based upon all our separation experiments using ROC curves, a methodology very commonly used in medical imaging and other fields but previously not demonstrated for particle separation devices.

6.2 Ongoing and Future Work

There is ongoing work to improve our ability to sort at optimal field and gradient values. We have recently designed a method that allows us finer control of the array-channel distance using height adjustment platforms that lift the channel to desired heights with a sensitivity of 1 μm as opposed to our previous sensitivity of .15 cm.

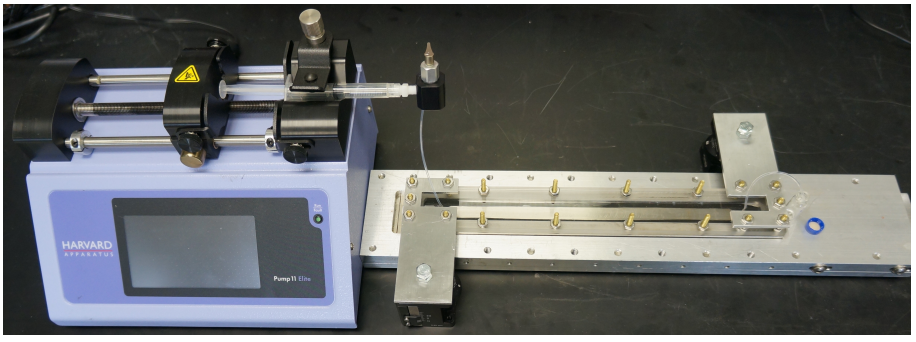

Figure 6.1: Using height adjustment platforms for finer control of array-channel distance.

In addition, the planar geometry of the array is potentially scalable to much larger sizes to easily increase throughput, which an important concern in nanoparticle separation devices. A scaled-down microfluidics version of the array could also be explored.

There is still much work to be done in terms of investigating the device's capabilities in separating other particle mixtures, especially more water-based ones relevant

for biomedical applications. Having obtained good results in separating particle distributions around average sizes differing by 10 nm, we would like to push the device further to sort mixtures with average sizes differing by less than 10 nm. In addition, future work could also be focused on figuring out the best ways to sort mixtures containing multiple particle distributions.

The work outlined here should continue to provide valuable insights for improving techniques of magnetic separation of nanoparticles in the future. These first investigations of the low flux side of the Halbach array have revealed qualities difficult to create using other means. Therefore, it may guide others in making use of its interesting magnetic characteristics for other applications as well.

Bibliography

[1] S. Odenbach. ***Colloidal Magnetic Fluids***. Springer, 2009 (page 1).

[2] E. Blums, A. Cebers, and M. Maiorov. ***Magnetic Fluids***. Berlin: Walter de Gruyter, 1997, p. 416 (page 1).

[3] K. M. Krishnan. **Biomedical Nanomagnetics: A Spin Through Possibilities in Imaging, Diagnostics, and Therapy**. *IEEE Transactions on Magnetics* 46.7 (2010), pp. 2523–2558. DOI: 10.1109/TMAG.2010.2046907 (page 1).

[4] X. Michalet, F. F. Pinaud, L. A. Bentolila, J. M. Tsay, S. Doose, J. J. Li, G. Sundaresan, A. M. Wu, S. S. Gambhir, and S. Weiss. **Quantum Dots for Live Cells, in Vivo Imaging, and Diagnostics**. 307.5709 (2005), pp. 538–544. DOI: 10.1126/science.1104274 (page 1).

[5] H. B. Na, I. C. Song, and T. Hyeon. **Inorganic Nanoparticles for MRI Contrast Agents**. *Advanced Materials* 21.21 (2009), pp. 2133–2148 (page 1).

[6] Q. A. Pankhurst, N. K. T. Thanh, S. K. Jones, and J. Dobson. **Progress in applications of magnetic nanoparticles in biomedicine**. *Journal of Physics D: Applied Physics* 42.22 (2009), p. 224001. DOI: 10.1088/0022-3727/42/22/224001 (page 1).

[7] A. Ito, M. Shinkai, H. Honda, and T. Kobayashi. **Medical application of functionalized magnetic nanoparticles**. *Journal of Bioscience and Bioengineering* 100.1 (2005), pp. 1–11 (page 2).

[8] J. S. Beveridge, M. R. Buck, J. F. Bondi, R. Misra, P. Schiffer, R. E. Schaak, and M. E. Williams. **Purification and Magnetic Interrogation of Hybrid Au-Fe3O4 and FePt-Fe3O4 Nanoparticles**. *Angewandte Chemie International Edition* 50.42 (2011), pp. 9875–9879. DOI: 10.1002/anie.201104829 (page 2).

[9] J. R. Stephens, J. S. Beveridge, and M. E. Williams. **Analytical methods for separating and isolating magnetic nanoparticles**. *Physical Chemistry Chemical Physics* 14.10 (2012), pp. 3280–3289. DOI: 10.1039/c2cp22982j (pages 3, 5).

[10] P. S. Williams, F. Carpino, and M. Zborowski. **Magnetic Nanoparticle Drug Carriers and Their Study by Quadrupole Magnetic Field-Flow Fractionation**. *Mol.Pharmaceutics* 6.5 (2009), pp. 1290–1306 (page 4).

[11] C. T. Yavuz et al. **Low-field magnetic separation of monodisperse Fe3O4 nanocrystals**. *Science* 314.5801 (2006), pp. 964–967. DOI: 10.1126/science.1131475 (page 4).

[12] G. D. Moeser, K. A. Roach, W. H. Green, T. Alan Hatton, and P. E. Laibinis. **High-gradient magnetic separation of coated magnetic nanoparticles**. *AIChE Journal* 50.11 (2004), pp. 2835–2848. DOI: 10.1002/aic.10270 (page 4).

[13] J. T. Mayo, S. L. Seung, C. T. Yavuz, W. W. Yu, A. Prakash, J. C. Falkner, and V. L. Colvin. **A multiplexed separation of iron oxide nanocrystals using variable magnetic fields**. *Nanoscale* 3.11 (2011), pp. 4560–4563. DOI: 10.1039/c1nr10671f (page 4).

[14] F. Carpino, L. Moore, M. Zborowski, J. Chalmers, and P. Williams. **Analysis of magnetic nanoparticles using quadrupole magnetic field-flow fractionation**. *Journal of Magnetism and Magnetic Materials* 293.1 (2005), pp. 546–552 (page 4).

[15] P. S. Williams, F. Carpino, and M. Zborowski. **Characterization of magnetic nanoparticles using programmed quadrupole magnetic field-flow fractionation**. *Philosophical Transactions of the Royal Society London, Series A (Mathematical, Physical and Engineering Sciences)* 368.1927 (2010), pp. 4419–4437. DOI: 10.1098/rsta.2010.0133 (page 4).

[16] P. S. Williams, F. Carpino, and M. Zborowski. **Quadrupole magnetic field-flow fractionation: A novel technique for the characterization of magnetic nanoparticles**. *Journal of Magnetism and Magnetic Materials* 311.1 (2007), pp. 383–387. DOI: 10.1016/j.jmmm.2006.11.162 (page 4).

[17] J. S. Beveridge, J. R. Stephens, A. H. Latham, and M. E. Williams. **Differential Magnetic Catch and Release: Analysis and Separation of Magnetic Nanoparticles**. *Analytical Chemistry* 81.23 (2009), pp. 9618–9624 (page 5).

[18] J. S. Beveridge, J. R. Stephens, and M. E. Williams. **Differential magnetic catch and release: experimental parameters for controlled separation of magnetic nanoparticles**. *Analyst* 136.12 (2011), pp. 2564–2571 (page 5).

[19] B. Teste, F. Malloggi, A.-L. Gassner, T. Georgelin, J.-M. Siaugue, A. Varenne, H. Girault, and S. Descroix. **Magnetic core shell nanoparticles trapping in a microdevice generating high magnetic gradient**. *Lab Chip* 11 (5 2011), pp. 833–840. DOI: 10.1039/C0LC00510J (page 5).

[20] N. Tri, K. Caldwell, and R. Beckett. **Development of Electrical Field-Flow Fractionation**. *Analytical Chemistry* 72.8 (2000), pp. 1823–1829. DOI: 10.1021/ac990822i (page 5).

[21] J. A. Jamison, K. M. Krueger, C. T. Yavuz, J. T. Mayo, D. LeCrone, J. J. Redden, and V. L. Colvin. **Size-Dependent Sedimentation Properties of Nanocrystals**. *ACS Nano* 2.2 (2008), pp. 311–319. DOI: 10.1021/nn700144m (page 5).

[22] C.-L. Wang, M. Fang, S.-H. Xu, and Y.-P. Cui. **Salts-Based Size-Selective Precipitation: Toward Mass Precipitation of Aqueous Nanoparticles**. *Langmuir* 26.2 (2010), pp. 633–638. DOI: 10.1021/la903986v (page 5).

[23] A. M. Al-Somali, K. M. Krueger, J. C. Falkner, and V. L. Colvin. **Recycling Size Exclusion Chromatography for the Analysis and Separation of Nanocrystalline Gold**. *Analytical Chemistry* 76.19 (2004), pp. 5903–5910. DOI: 10.1021/ac049355h (page 5).

[24] S. F. Sweeney, G. H. Woehrle, and J. E. Hutchison. **Rapid Purification and Size Separation of Gold Nanoparticles via Diafiltration**. *Journal of the American Chemical Society* 128.10 (2006), pp. 3190–3197. DOI: 10.1021/ja0558241 (page 5).

[25] K. Halbach. **Design of permanent multipole magnets with oriented rare earth cobalt material**. *Nuclear Instruments and Methods* 169.1 (1980), pp. 1–10 (page 6).

[26] R. Bjork, C. R. H. Bahl, A. Smith, and N. Pryds. **Comparison of adjustable permanent magnetic field sources**. *Journal of Magnetism and Magnetic Materials* 322.22 (2010), pp. 3664–3671. DOI: 10.1016/j.jmmm.2010.07.022 (page 6).

[27] J. Hilton and S. McMurry. **An adjustable linear Halbach array**. *Journal of Magnetism and Magnetic Materials* 324.13 (2012), pp. 2051 –2056. DOI: http://dx.doi.org/10.1016/j.jmmm.2012.02.014 (page 6).

[28] J. C. Mallinson. **One-sided fluxes-a magnetic curiosity?** *IEEE Transactions on Magnetics* Mag-9.4 (1973), pp. 678–682 (page 6).

[29] P. Babinec, A. Krafck, M. Babincova, and J. Rosenecker. ***Dynamics of magnetic particles in cylindrical Halbach array: implications for magnetic cell separation and drug targeting***. 2010 (page 7).

[30] M. E. Hayden and U. O. Hafeli. **'Magnetic bandages' for targeted delivery of therapeutic agents**. *Journal of Physics: Condensed Matter* 18.38 (2006). DOI: 10.1088/0953-8984/18/38/S23 (page 7).

[31] A. Sarwar, A. Nemirovski, and B. Shapiro. **Optimal Halbach permanent magnet designs for maximally pulling and pushing nanoparticles**. *Journal of Magnetism and Magnetic Materials* 324.5 (2012), pp. 742–754. DOI: 10.1016/j.jmmm.2011.09.008 (page 7).

[32] M. Hoyos, L. Moore, P. S. Williams, and M. Zborowski. **The use of a linear Halbach array combined with a step-SPLITT channel for continuous sorting of magnetic species**. *Journal of Magnetism and Magnetic Materials* 323.10 (2011), pp. 1384–1388. DOI: 10.1016/j.jmmm.2010.11.051 (page 7).

[33] Q. A. Pankhurst, J Connolly, and J. S K Jones and. **Applications of magnetic nanoparticles in biomedicine**. *Journal of Physics D: Applied Physics* 36.13 (2003), R167 (page 9).

[34] R. C. O'Handley. ***Modern Magnetic Materials: Principles and Applications***. Wiley, 1999 (page 9).

[35] E. du Tremolet de Lacheisserie, D. Gignoux, and M. Schlenker. ***Magnetism: Fundamentals, Materials and Applications***. Springer, 2002 (page 9).

[36] B. D. Cullity and C. D. Graham. ***Introduction to Magnetic Materials***. Wiley, 2009 (pages 9, 23).

[37] F. Himpsel, J. Ortega, G. Mankey, and R. Willis. **Magnetic nanostructures**. *Advances in physics* 47.4 (1998), pp. 511–597 (page 12).

[38] C. P. Bean and J. D. Livingston. **Superparamagnetism**. *Journal of Applied Physics* 30.4 (1959), S120–S129 (page 13).

[39] R. E. Rosensweig. ***Ferrohydrodynamics***. Mineola, N.Y.: Dover Publications, 1997 (pages 14, 16).

[40] G. De Las Cuevas, J. Faraudo, and J. Camacho. **Low-Gradient Magnetophoresis through Field-Induced Reversible Aggregation**. *The Journal of Physical Chemistry C* 112.4 (2008), pp. 945–950. DOI: 10.1021/jp0755286 (pages 16, 31).

[41] A. Demortiere, P. Panissod, B. P. Pichon, G. Pourroy, D. Guillon, B. Donnio, and S. Begin-Colin. **Size-dependent properties of magnetic iron oxide nanocrystals**. *Nanoscale* 3 (1 2011), pp. 225–232. DOI: 10.1039/C0NR00521E (page 16).

[42] D. S. Sivia. ***Elementary scattering theory : for X-ray and neutron users***. Oxford; New York: Oxford University Press, 2011, p. 201 (page 17).

[43] O. Glatter and O. Kratky. ***Small angle x-ray scattering***. Place of Publication: London, UK. Country of Publication: UK.: Academic Press, 1982 (page 17).

[44] D. I. Svergun, L. A. Fegin, and G. W. Taylor. ***Structure Analysis by Small-angle X-ray and Neutron Scattering***. Kluwer Academic Pub, 1987 (page 17).

[45] C. Windsor. **An Introduction to Small-Angle Neutron-Scattering**. *Journal of Applied Crystallography* 21 (1988), pp. 582–588 (page 19).

[46] D. Meeker. *Finite element method magnetics*. Version 4.2 (1 April 2009 Build). 2010 (page 22).

[47] S. Sun and H. Zeng. **Size-Controlled Synthesis of Magnetite Nanoparticles**. *Journal of the American Chemical Society* 124.28 (2002), pp. 8204–8205. DOI: 10.1021/ja026501x (page 36).

[48] H.-C. Gu, L. Zhang, and R. He. **Oleic acid coating on the monodisperse magnetite nanoparticles**. *Applied Surface Science* 253.5 (2006), pp. 2611–2617. DOI: 10.1016/j.apsusc.2006.05.023 (pages 36, 46).

[49] Z. Feng, S. Zhu, D. R. M. de Godoi, A. C. S. Samia, and D. Scherson. **Adsorption of Cd2+ on Carboxyl-Terminated Superparamagnetic Iron Oxide Nanoparticles**. *Analytical Chemistry* 84.8 (2012), pp. 3764–3770 (page 36).

[50] A. Sasaki. **Size Distribution Analysis of Nanoparticles Using Small Angle X-ray Scattering Technique**. *The Rigaku Journal* 22.1 (2005), pp. 31–38 (page 37).

[51] W. Rasband. *ImageJ*. U. S. National Institutes of Health, Maryland, USA, 1997-2014. URL: http://imagej.nih.gov/ij/ (page 37).

[52] R. Bond. "**Liquid Phase Small Angle X-ray Scattering of Iron Oxide Nanoparticles**". Senior Thesis, Oberlin College. 2014 (page 39).

[53] *NANO-Solver: Particle size and pore size analysis software*. Rigaku Corporation. URL: http://www.rigaku.com/service/software/nanosolver (page 40).

[54] S. Kline. **Reduction and analysis of SANS and USANS data using Igor Pro**, journal=Journal of applied crystallography. 39.6 (2006), pp. 895–900 (page 41).

[55] K. Hasz. "**Polarization Analyzed Small Angle Neutron Scattering of Ferrite Nanoparticles**". Honors Thesis, Oberlin College. 2014 (page 41).

[56] **Receiver Operating Characteristic Analysis in Medical Imaging**. *Journal of the ICRU* 8.1 (2008). DOI: 10.1093/jicru/ndn003 (page 61).

[57] C. Metz. **Roc Methodology in Radiologic Imaging**. *Investigative radiology* 21.9 (1986), pp. 720–733 (page 61).

[58] J. A. Swets. **Measuring the Accuracy of Diagnostic Systems**. *Science* 240.4857 (1988), pp. 1285–1293 (page 61).

Appendix A

Solidworks CAD Designs

Figures of CAD designs of the channel base for the older toluene-compatible glass channel, and the top and bottom plates for the new water-compatible Plexiglas channel have been included in this Appendix.

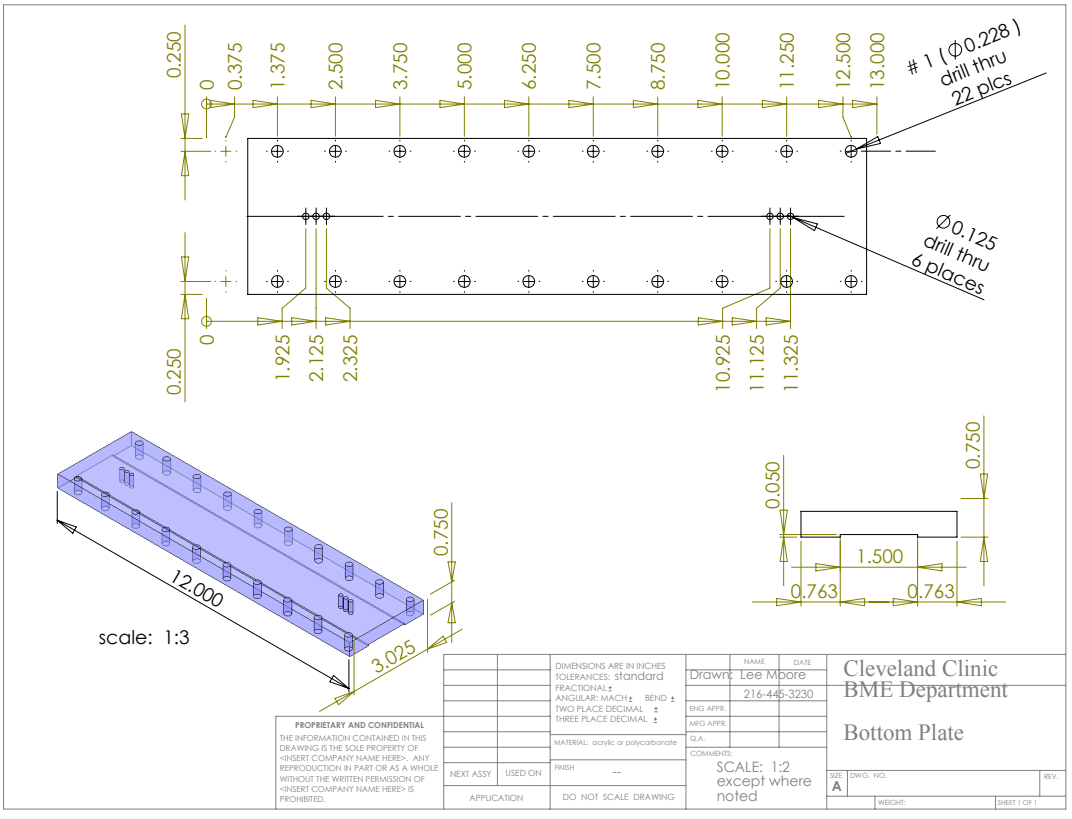

Figure A.1: Design of Plexiglas channel base for the toluene-compatible glass channel, with holes for 22 large aluminium screws to hold the system tight and prevent leaks of nanoparticle suspensions.

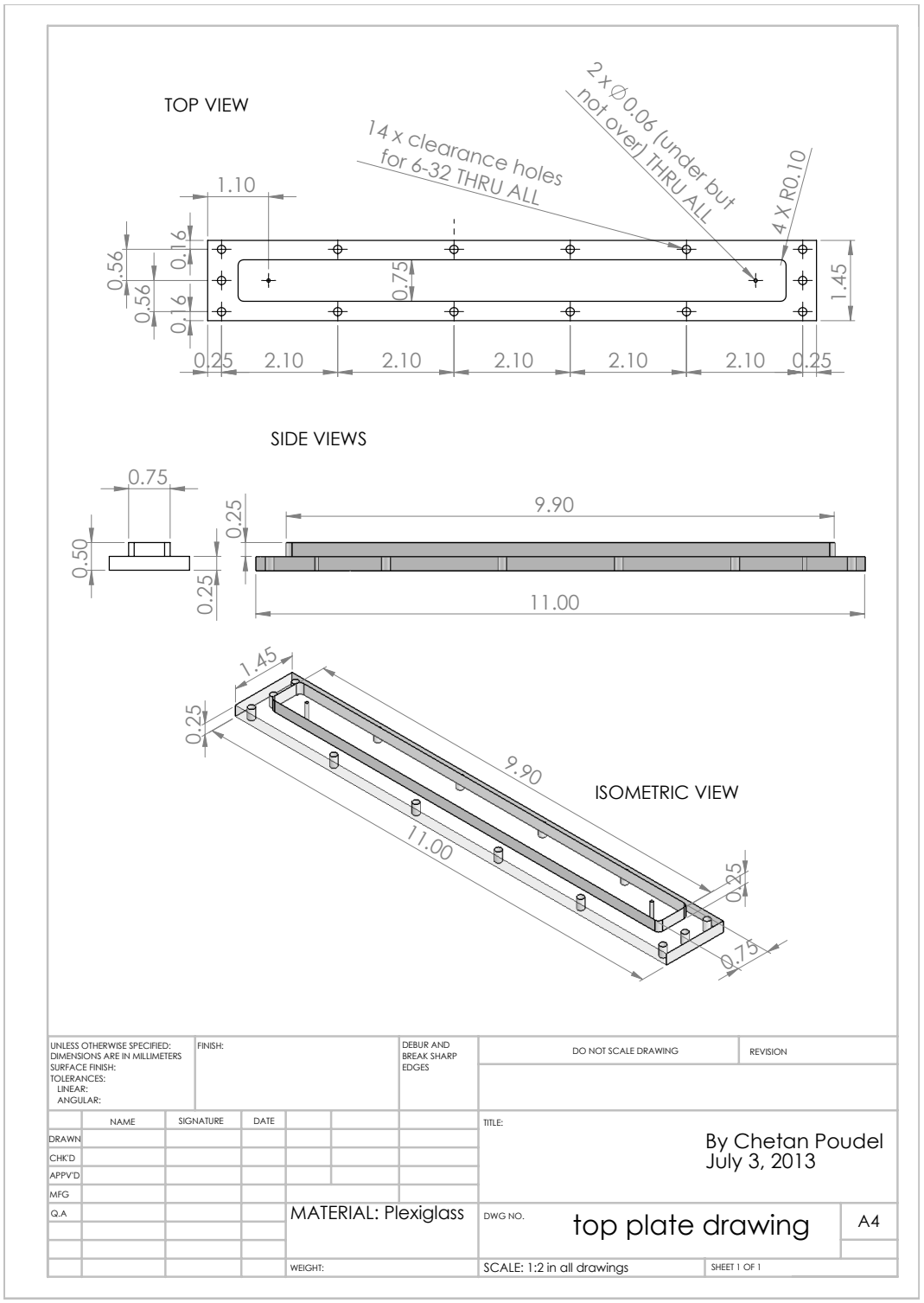

Figure A.2: Design of Plexiglas top plate for the water-compatible flow channel.

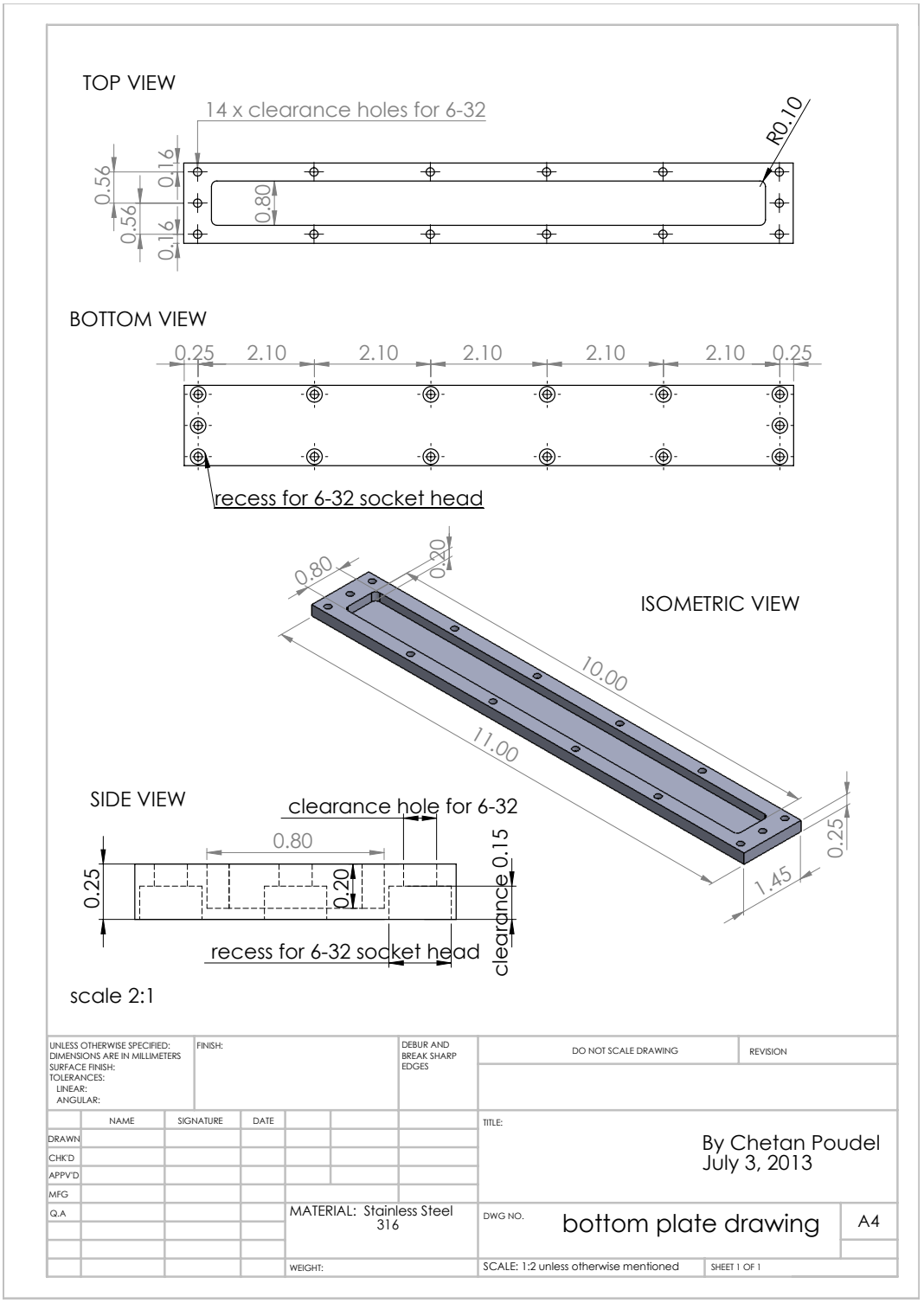

Figure A.3: Design of stainless steel bottom plate for the water-compatible flow channel such that the Plexiglas top plate fits tightly into .